

Probable Dormant Neutron Star in a Short-Period Binary System

Tsevi Mazeh,^{1*} Simchon Faigler,¹ Dolev Bashi,¹ Sahar Shahaf,^{1,2} Niv Davidson,¹ Matthew Green,¹ Roy Gomel,¹ Dan Maoz,¹ Amitay Sussholz,¹ Subo Dong,³ Haotong Zhang,⁴ Jifeng Liu,⁴ Song Wang,⁴ Ali Luo,⁴ Zheng Zheng,⁵ Na'ama Hallakoun,² Volker Perdelwitz,^{6,7} David W. Latham,⁸ Ignasi Ribas,^{9,10} David Baroch,^{9,10} Juan Carlos Morales,^{9,10} Evangelos Nagel,^{7,11} Nuno C. Santos,^{12,13} David R. Ciardi,¹⁴ Jessie L. Christiansen,¹⁴ Michael B. Lund,¹⁴ Joshua N. Winn¹⁵

¹*School of Physics and Astronomy, Tel Aviv University, Tel Aviv, 6997801, Israel*

²*Department of particle physics and astrophysics, Weizmann Institute of Science, Rehovot 7610001, Israel*

³*Kavli Institute for Astronomy and Astrophysics, Peking University, Yi He Yuan Road 5, Hai Dian District, Beijing 100871, People's Republic of China*

⁴*National Astronomical Observatories, CAS, People's Republic of China*

⁵*Department of Physics and Astronomy, University of Utah, 115 South 1400 East, Salt Lake City, UT 84112, USA*

⁶*Department of physics, Ariel University*

⁷*Hamburger Sternwarte, Universität Hamburg, Gojenbergsweg 112, 21029 Hamburg, Germany*

⁸*Center for Astrophysics Harvard & Smithsonian, 60 Garden St., Cambridge, Mass., USA*

⁹*Institut de Ciències de l'Espai (ICE, CSIC), Campus UAB, c/ Can Magrans s/n, E-08193 Bellaterra, Barcelona, Spain*

¹⁰*Institut d'Estudis Espacials de Catalunya (IEEC), c/ Gran Capità 2- 4, E-08034 Barcelona, Spain*

¹¹*Thüringer Landessternwarte Tautenburg, Sternwarte 5, 07778 Tautenburg, Germany*

¹²*Instituto de Astrofísica e Ciências do Espaço, Universidade do Porto, CAUP, Rua das Estrelas, 4150-762 Porto, Portugal*

¹³*Departamento de Física e Astronomia, Faculdade de Ciências, Universidade do Porto, Rua do Campo Alegre, 4169-007 Porto, Portugal*

¹⁴*NASA Exoplanet Science Institute — Caltech IPAC*

¹⁵*Department of Astrophysical Sciences, Princeton University, Princeton, NJ 08540, USA*

Accepted XXX. Received YYY; in original form ZZZ

ABSTRACT

We have identified 2XMM J125556.57+565846.4, at a distance of 600 pc, as a binary system consisting of a normal star and a probable dormant neutron star. Optical spectra exhibit a slightly evolved F-type single star, displaying periodic Doppler shifts with a 2.76-day Keplerian circular orbit, with no indication of light from a secondary component. Optical and UV photometry reveal ellipsoidal modulation with half the orbital period, due to the tidal deformation of the F star. The mass of the unseen companion is constrained to the range of 1.1–2.1 M_{\odot} at 3σ confidence, with the median of the mass distribution at 1.4 M_{\odot} , the typical mass of known neutron stars. A main-sequence star cannot masquerade as the dark companion. The distribution of possible companion masses still allows for the possibility of a very massive white dwarf. The companion itself could also be a close pair consisting of a white dwarf and an M star, or two white dwarfs, although the binary evolution that would lead to such a close triple system is unlikely. Similar

ambiguities regarding the certain identification of a dormant neutron star are bound to affect most future discoveries of this type of non-interacting system. If the system indeed contains a dormant neutron star, it will become, in the future, a bright X-ray source and afterwards might even host a millisecond pulsar.

Key words: binaries: close – binaries: spectroscopic – stars:neutron

1 INTRODUCTION

Neutron stars are among the most exotic known astronomical objects, with typical masses of 1.2–2 M_{\odot} (e.g., [Antoniadis et al. 2016](#); [Özel & Freire 2016](#)) and radii of ~ 10 km, resulting in mass densities on the order of 10^{14} g/cc (e.g., [Özel & Freire 2016](#)), similar to atomic-nucleus density. They are formed by supernova explosions of stars with initial masses larger than $\sim 8 M_{\odot}$, and therefore are quite rare ([Tauris & van den Heuvel 2006](#)).

Most of the known neutron stars are young pulsars, discovered by virtue of their periodic radio pulses, which reveal their fast rotation (e.g., [Faucher-Giguère & Kaspi 2006](#)). Neutron stars cease emitting radio pulses after much of their rotational spin energy has been radiated away ([Bransgrove et al. 2018](#)). However, a neutron star can be revived as a pulsar if it resides in a binary system. When the companion leaves the main sequence (MS), its outer layers expand until they are pulled onto the neutron star, if the two stars are close enough. The mass transferred onto the compact object can generate a high X-ray luminosity, while the associated angular momentum increases the spin rate of the neutron star ([Bhattacharya & van den Heuvel 1991](#)). Indeed, some neutron stars are visible as bright X-ray sources (e.g., [Paul 2017](#)), and many others as ‘revived’ millisecond pulsars ([Manchester 2017](#)).

During the long MS lifetime of the companion, the neutron star is extremely faint in all electromagnetic bands, making this type of system difficult to discover. The binary appears as a single optical-band star, without any X-ray or radio emission. The binarity of such a system can only be revealed through gravitational interactions with the unseen, relatively massive, companion. In such cases, however, one must rule out the possibility that the companion is a fainter MS star, before concluding that the companion is a compact stellar remnant: a white dwarf, a neutron star, or a black hole. Most if not all recent efforts to detect compact binary companions in this manner ([Abdul-Masih et al. 2020](#); [Rivinius et al. 2020a](#)) have not been able to definitively rule out the possibility that the secondary is a MS or a sub-giant star, (e.g., [Mazeh & Faigler 2020](#); [El-Badry et al. 2022a,c](#)).

* E-mail: mazeh@tauex.tau.ac.il

In this paper, we identify 2XMM J125556.57+565846.4, hereafter J1255, a slightly evolved F-type star, as a likely MS plus neutron star system. The system was selected based on large radial-velocity (RV) differences ($RV_{\max} - RV_{\min}$) seen in the LAMOST stellar RV public database. Follow-up spectroscopic observations reveal J1255 as a 2.76-day single-lined spectroscopic binary system. *TESS* optical and Swift-UVOT ultraviolet photometry display ellipsoidal modulation with half the orbital period, due to the tidal deformation of the F star. The data constrain the mass of the unseen companion to a range $1.1\text{--}2.1 M_{\odot}$ (3σ), consistent with the typical mass of the known neutron stars. This is the first dormant neutron-star candidate discovered in a short-period binary.

Just before submission of the paper, the *Gaia* large sample of spectroscopic binaries became available (Gaia Collaboration et al. 2022). The catalog includes an orbit for J1255, Gaia DR3 1577114915964797184, consistent with our spectroscopic orbit.

Section 2 presents the radial-velocity observations of the system, Section 3 the optical and UV photometry of the binary, Section 4 derives the stellar parameters of the primary and Section 5 derives the companion mass. We discuss our results in Section 6.

2 RADIAL VELOCITIES OF J1255

2.1 LAMOST radial velocities

Our initial search for compact objects was based on the LAMOST (Cui et al. 2012) stellar RV DR6 database,¹ which includes on the order of 10^6 sources with at least two measurement epochs. We searched for stars showing large RV differences between the available measurements, which could indicate binary motion with a massive companion. The search identified 955 882 stars with more than one RV measurement; a histogram of the number of epochs per star is presented in Fig. 1. Some of these stars display large RV differences, as seen in Fig. 2.

One such, relatively bright ($V=11.9$) star — TIC (*TESS* Input Catalog) 150388416 (Stassun et al. 2019),² the faint X-ray source 2XMM J125556.57+565846.4 (Watson et al. 2009; Webb et al. 2020) (hereafter J1255),

has two LAMOST measurements separated by 185 km s^{-1} , as seen in the figure, suggesting a large-amplitude RV modulation. The LAMOST spectrum of J1255, shown in Fig. 3, indicates a normal F-type star.

¹ <http://dr6.lamost.org/v1/>

² <https://tess.mit.edu/science/tess-input-catalogue/>

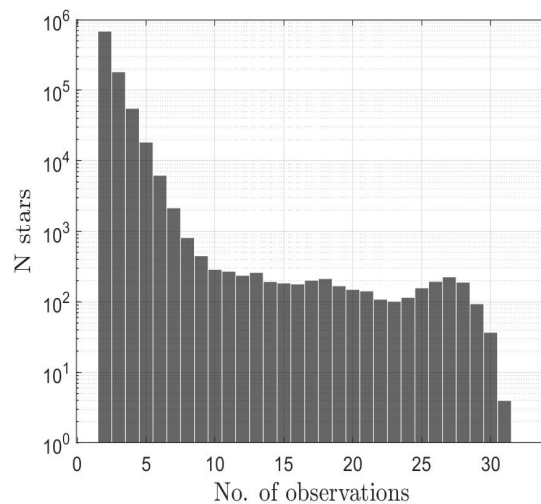


Figure 1. Distribution of number of RV epochs for stars with multiple measurements in LAMOST DR6

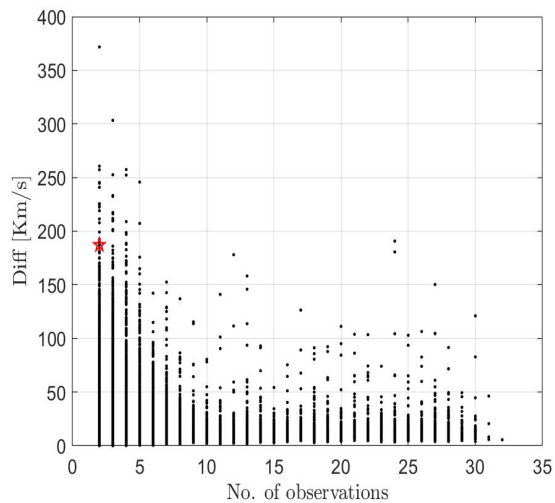


Figure 2. RV differences vs. number of observations in LAMOST DR6. Red star represents J1255.

The *TESS* photometry (see Section 3.1 below) indicated the star might be a good candidate for our search for dormant compact objects.

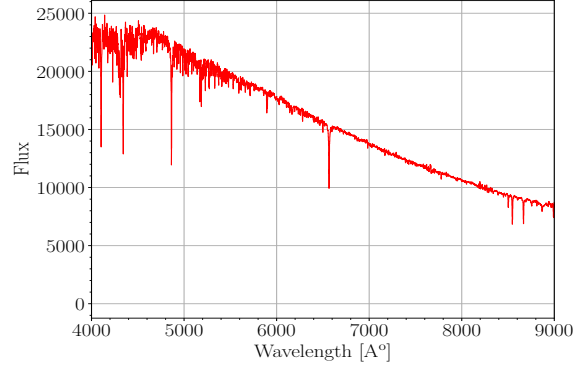


Figure 3. LAMOST spectrum of J1255. Flux in arbitrary units.

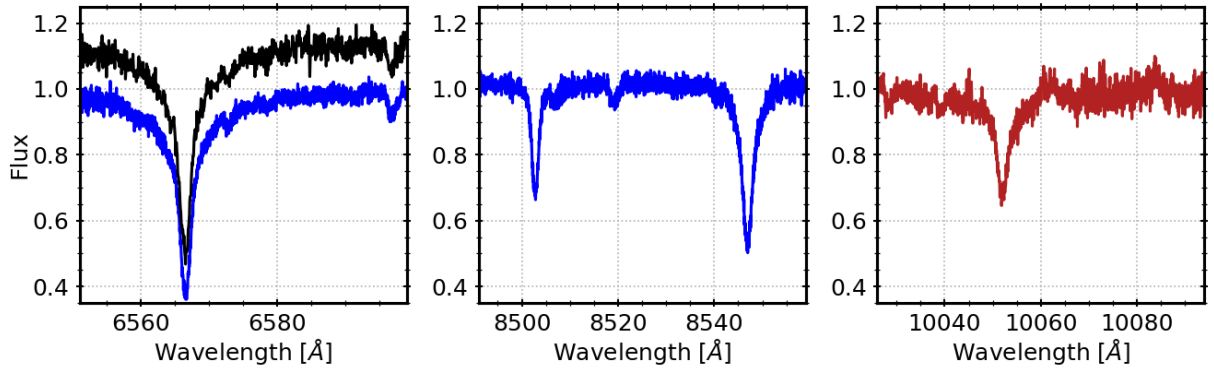


Figure 4. TRES (black), CARMENES-VIS (blue) and CARMENES-NIR (red) coadded spectra. The spectra include the $H\alpha$ line (left), two of the Ca II triplet lines (middle), and the Pa- δ line (right).

2.2 TRES and CARMENES radial velocities

To derive the binary period and the RV amplitude, we monitored J1255 with two spectroscopic facilities. We obtained 14 spectra with TRES³ — the Tillinghast Reflector Echelle Spectrograph,⁴ mounted on the 1.5 m telescope at the Fred Lawrence Whipple Observatory, Arizona. TRES is a fiber-fed echelle spectrograph with wavelength coverage from 3900 to 9100 Å, spanning 51 echelle orders at a resolution of $R \approx 44000$. Wavelength solutions are provided by ThAr-lamp exposures that bracket each observation. The observations are reduced as per Buchhave et al. (2010). RVs were obtained by correlating the orders that contain enough spectral information with the observed spectrum that has the highest Signal-to-Noise-Ratio (SNR). The cross-correlation function (CCF) was calculated independently for each spectral order. The RVs and their uncertainties were derived from the combined CCF (see Zucker 2003a).

³ <http://tdc-www.harvard.edu/instruments/tres/>

⁴ <https://exofop.ipac.caltech.edu/tess/TRESnote.pdf>

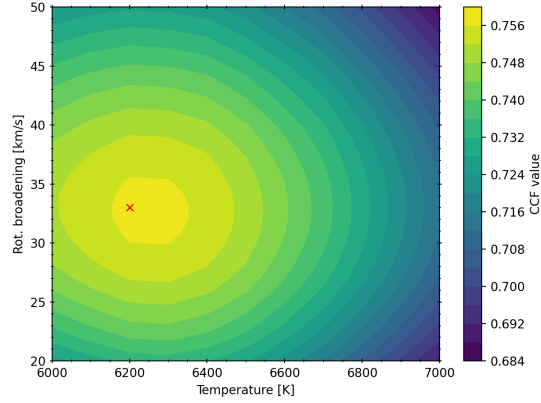


Figure 5. Search for the best template to derive the RVs of the CARMENES spectra performed with TODMOR. The color code indicates the peak value of the cross-correlation function, obtained for different stellar rotations and temperatures, with the red cross indicating the best values. Note the shallow peak along the rotation axis.

Five additional spectra were obtained in February 2021 with CARMENES⁵ (Quirrenbach et al. 2016, 2018), attached to the Cassegrain focus of the 3.5 m telescope at Calar Alto observatory, Almería, Spain. CARMENES consists of a pair of cross-dispersed echelle spectrographs, the visual channel (VIS) covering a wavelength range from 5200 to 9200 Å with $R \approx 94600$, and the near-infrared channel (NIR), which covers a wavelength range from 9600 to 17100 Å at $R \approx 80400$. Both channels use Fabry-Pérot etalons and hollow-cathode emission-line lamps for wavelength calibration (Schäfer et al. 2018). The data reduction of CARMENES observations is performed by the caracal pipeline (Caballero et al. 2016), which corrects for bias, flat-fielding, and cosmic ray events, performs wavelength calibration, and extracts one-dimensional spectra. The spectra were corrected for telluric contamination following the procedure described by (Nagel et al. 2022). Fig. 4 shows three of the spectral ranges covered by CARMENES. The panel with H α shows also the TRES spectrum in that range.

To analyze the optical CARMENES spectra, we first adopted a theoretical template from the library of PHOENIX stellar models (Husser et al. 2013) that best fit the observed spectral features. We explored a grid of values for effective temperature and spectral line broadening (approximately equivalent to the projected rotation velocity, $v \sin i_{\text{rot}}$), where i_{rot} is the inclination of the stellar rotation axis, looking for a combination that maximized the cross correlation, as illustrated by Fig. 5. The best-fitting template parameters and 1σ uncertainties are $T_{\text{eff}} = 6280 \pm 60$ K and $v \sin i_{\text{rot}} = 32.3 \pm 0.5$ km s⁻¹. A rotational broadening profile (Gray 1992) was applied to account for the stellar rotation while adopting a limb-darkening coefficient from Claret & Bloemen (2011). This template was then used to derive the CARMENES RVs.

⁵ <https://carmenes.caha.es/ext/instrument/index.html>

Table 1. RVs of J1255.

Time BJD-2450000	RV km s ⁻¹	RV	
		Uncertainty km s ⁻¹	Instrument
6424.556	-99.94	6.47	L
7474.662	85.77	5.42	L
9202.041	-187.61	0.87	T
9204.020	-68.98	1.18	T
9212.027	-18.21	0.64	T
9217.036	-5.49	0.65	T
9217.990	-103.99	0.16	T
9218.982	-157.11	0.64	T
9219.985	3.43	0.49	T
9231.001	3.60	0.37	T
9231.960	-139.65	0.38	T
9245.968	-172.33	0.46	T
9264.394	80.09	0.94	C
9264.594	51.66	0.34	C
9264.648	41.47	0.37	C
9264.720	26.81	0.44	C
9272.563	90.05	0.37	C
9565.039	3.62	0.53	T
9582.028	-31.46	0.29	T
9587.027	0.00	0.53	T
9591.986	-91.45	0.56	T

L-LAMOST, T-TRES, C-CARMENES

2.3 Orbital solution

The RVs measured by the three instruments — LAMOST, TRES and CARMENES — are listed in Table 1, together with their 1σ uncertainties. The TRES velocities are relative to the RV at BJD 2459587.

To derive an orbital solution for J1255, we applied the `exoplanet` package (Foreman-Mackey et al. 2021a) with the probabilistic model in `PyMC3` (Salvatier et al. 2016), allowing for different RV offsets of the three spectrographs. We first explored a non-zero eccentricity model, finding insignificant eccentricity at a 2σ limit of $e < 8 \times 10^{-3}$. We therefore adopted a circular model, (zero eccentricity and zero longitude of the periastron), with an uninformative prior for the semi-amplitude, K , orbital period, P , the time of inferior conjunction, T_0 , and γ , the RV of the center of mass of the system. Posterior distributions of the fitted parameters are shown in Fig. 6, and the adopted parameters are given in Table 2. The best-fit model, together with the data and residuals, are plotted in Fig. 7 and 8.

To better constrain the possibility of a long-term RV trend, we attempted to include a linear trend in the solution. Based on the TRES dataset, we constrain the slope to $-0.0015 < a < 0.0030$ km s⁻¹/day at the 2σ level, indicating that any such a linear trend is insignificant, within the range accessible to our precision and data time span.

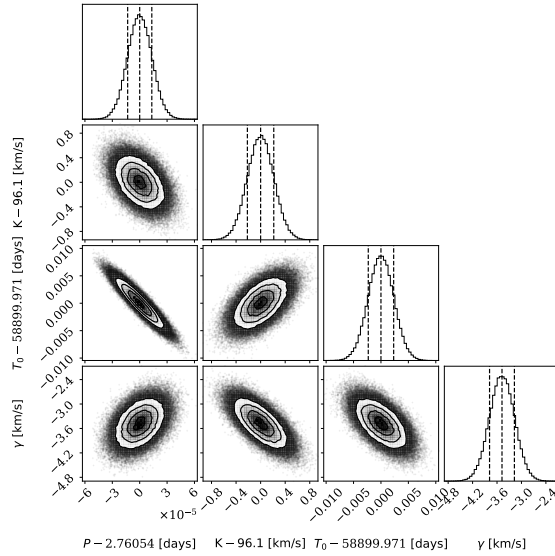


Figure 6. MCMC posterior distributions of the orbital parameters — period, P , Semi-amplitude, K , time of inferior conjunction, T_0 [BJD-2400000] and center-of-mass RV, γ , based on the CARMANES RV offset. Off-diagonal sub-plots present the joint distributions with contours, and diagonal elements show the probability distribution of each parameter, with percentiles of 16%, 50% and 84%, denoted by vertical dashed lines.

Table 2. Orbital solution for J1255.

	P [day]	T_0 [BJD]	K [km s $^{-1}$]	γ [km s $^{-1}$]
	2.760541	2458899.970	96.1	-3.4
\pm	0.000013	0.002	0.2	0.3

Just before submission of the paper, the *Gaia* orbit of J1255, *Gaia* DR3 1577114915964797184, became available. Their elements — period of $2.760586 \pm 4.9 \times 10^{-5}$ d, semi-amplitude of 96.2 ± 1.3 km s $^{-1}$ and eccentricity of 0.019 ± 0.011 ([Gaia Collaboration et al. 2022](#)), are consistent with our spectroscopic orbit.

3 PHOTOMETRIC MODULATION OF J1255 — *TESS* AND UVOT

3.1 *TESS*

J1255 was observed by *TESS* — the Transiting Exoplanet Survey Satellite ([Ricker et al. 2015](#)) during Sectors 15 and 22. Each sector includes observations for 27.4 days, with full-frame images recorded continuously at a cadence of ~ 30 min. A 1.5-day gap at the midpoint of each sector is a result of the data downlink from the satellite. The light curve of J1255 was extracted from the full-frame images using the *eleanor* package ([Feinstein et al. 2019](#)), and is plotted in the upper panels of Fig. 9.

The *TESS* variability is dominated by a periodic signal at half the orbital period, consistent with an ellipsoidal modulation caused by the tidal distortion of the primary star induced by the gravity

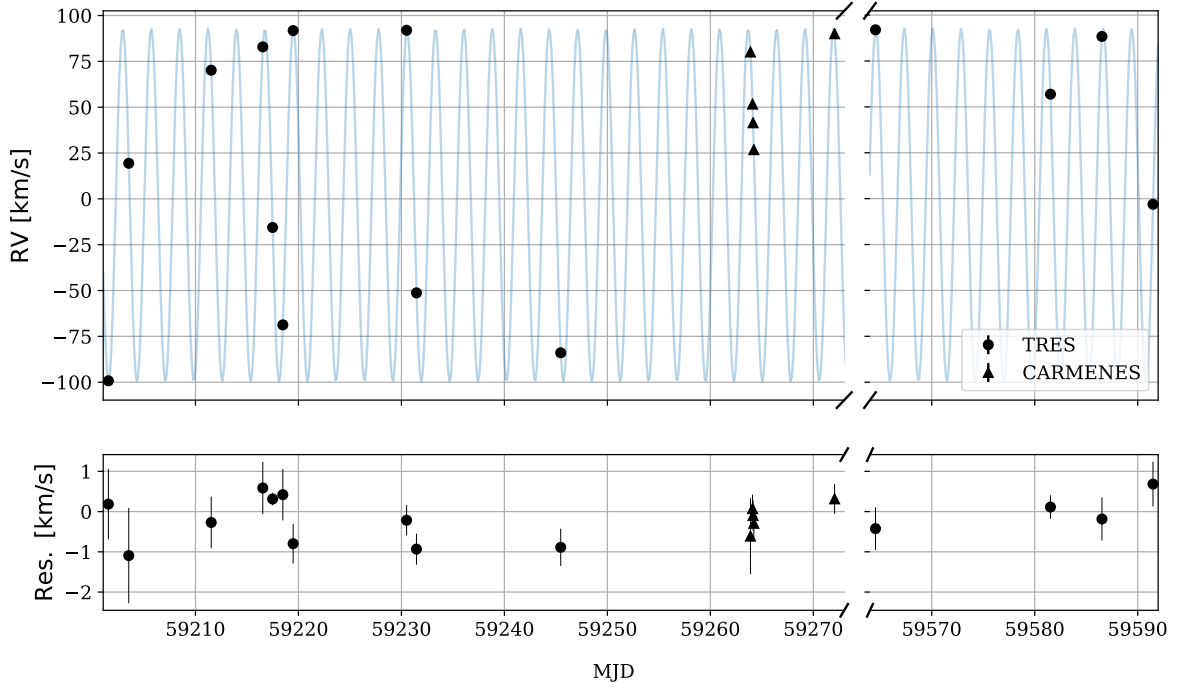


Figure 7. Orbital solution for J1255. *Top* — best model with the RV measurements. For display purposes, we have excluded LAMOST measurements, because of their large time span. *Bottom* — residuals from the model.

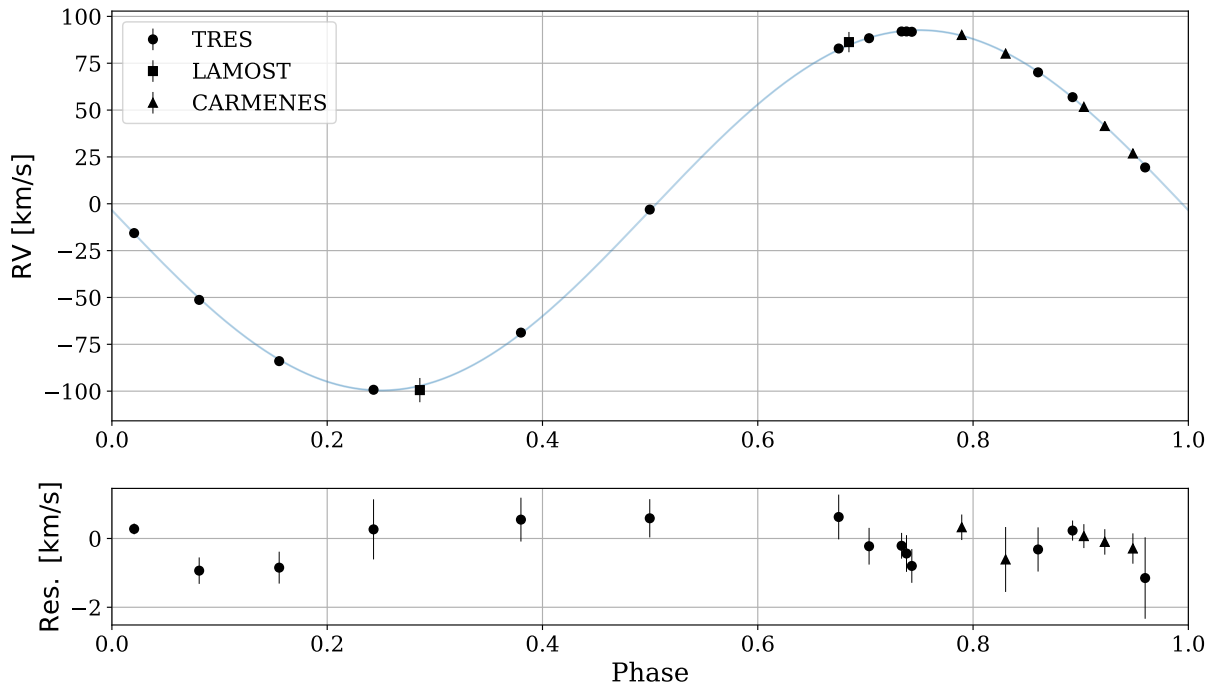


Figure 8. *Top* — radial velocities of J1255, derived from the TRES, CARMENES, and LAMOST spectra, together with the orbital solution, folded with the $P=2.760549$ d orbital period. *Bottom* — residuals.

of the unseen companion (Kopal 1959; Morris 1985; Morris & Naftilan 1993). This variability, at the level of 5 ppt (parts per thousands of the average stellar luminosity), is plotted and modeled in Fig. 9 using the first three harmonics of the orbital period and the phase derived from the RVs in Section 2.3. Low-frequency systematic effects were filtered using a Fourier comb, applied at frequencies lower than $0.25\times$ the orbital frequency, simultaneous with the harmonic fit (Faijler & Mazeh 2011).

Fig. 9 also shows the residuals from the fit, which display some additional variability at a level of 2–3 ppt, most clearly in the data from Sector 15. The extra variability, displayed in the middle panels of the figure, is not strictly periodic, and therefore we opted to present its autocorrelation (ACF), as in McQuillan, Aigrain & Mazeh (2013). The ACF shows that the variability is indeed strongly correlated with itself at earlier times, at a typical lag that is similar to the orbital period. This probably originates from stellar rotation, as observed in many stars by recent space missions (McQuillan et al. 2014). The stellar rotation period is equal or almost equal to the orbital period, apparently because stellar rotation tends to be synchronized with orbital period at such short periods (e.g., Mazeh 2008).

For our canonical measurement of the ellipsoidal amplitude, we use only Sector 22, in which the residuals are significantly smaller and less correlated. The phase-folded data from Sector 22 are shown in Fig. 10, along with the best-fit two-harmonic model. As before, the period and phase of the fit were fixed at the RV orbital-solution values.

The cosine and sine amplitudes of the two harmonics ($a_{1c}, a_{1s}, a_{2c}, a_{2s}$) in units of the median flux of the system are given in the upper part of Table 3. Also given are the total amplitudes of these two harmonics (A_1 and A_2). The ellipsoidal amplitude of the best-fit model is 4.27 ± 0.05 ppt.

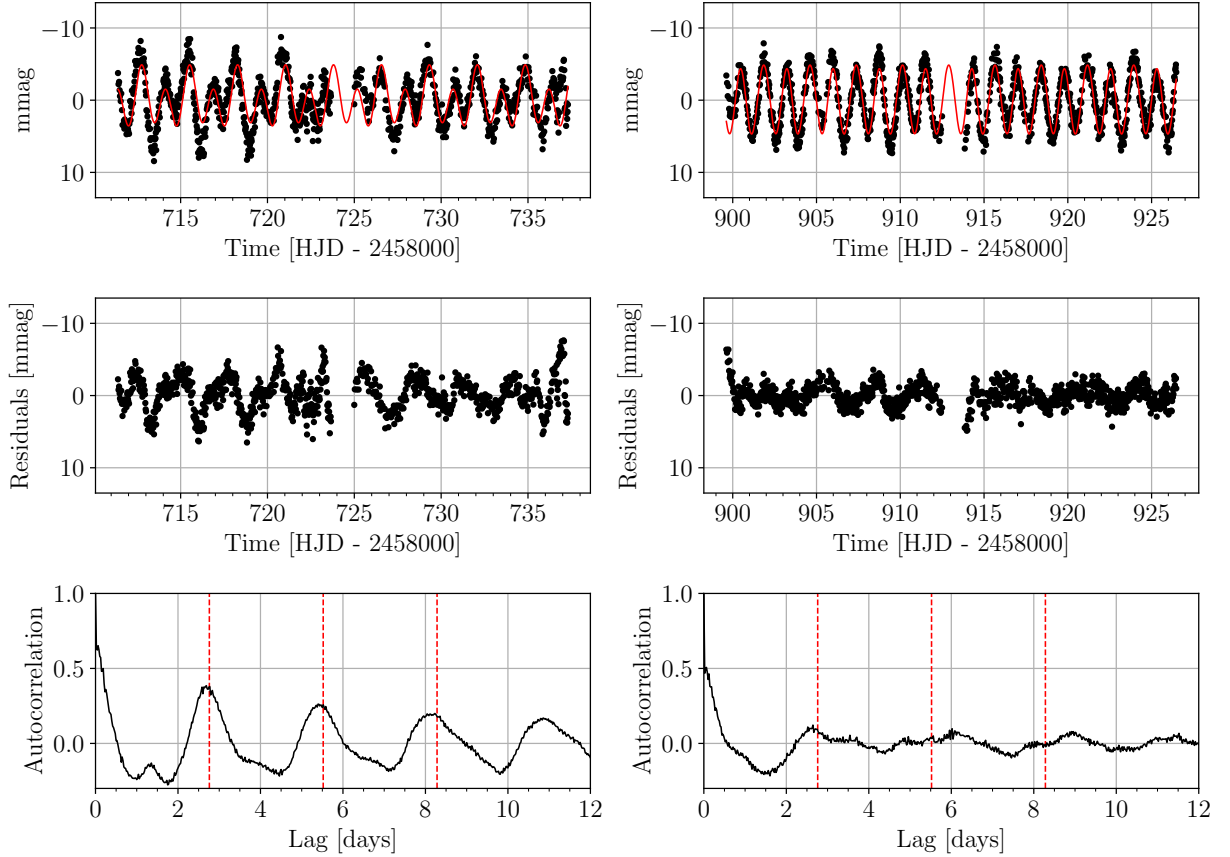
3.1.1 Beaming modulation?

Note that we expect another photometric modulation — the beaming effect, induced by the radial velocity of the optical star (e.g., Zucker et al. 2007; Faijler & Mazeh 2011, 2015), which appears as a sine function of the orbital phase for a circular orbit. For a sun-like star in the *TESS* band the amplitude is $\sim 4V_{\text{orb}}/c$, where V_{orb} is the orbital velocity and c is the light velocity. In our case the expected amplitude is ~ 1.3 ppt. The observed modulation, represented by the a_{1s} coefficient, is only ~ 0.5 ppt.

Apparently, the other variability, probably due to the stellar spots, masks the full manifestation of the beaming modulation. We probably need a longer time span, like the *Kepler* light curves

Table 3. Harmonic amplitudes of J1255 in terms of the median flux.

	a_{1c} [ppt]	a_{1s} [ppt]	A_1 [ppt]	a_{2c} [ppt]	a_{2s} [ppt]	A_2 [ppt]
TESS	0.501	0.494	0.703	-4.266	-0.086	4.267
±	0.054	0.054	0.054	0.054	0.054	0.054
UVOT	2.681	-5.042	5.71	-4.194	7.322	8.438
±	1.606	1.514	1.535	1.532	1.59	1.576


Figure 9. *TESS* photometry obtained from Sectors 15 (left) and 22 (right). *Top* — light curve in mmag (black), after removal of long-term trend, and a three-harmonic model applied to that sector (red). Orbital period and phase were held fixed at the RV-derived values. *Middle* — residuals from the models. *Bottom* — autocorrelation function of the residuals, where red, dashed, vertical lines mark 1 \times , 2 \times and 3 \times the orbital period.

(e.g., [Faigler et al. 2012, 2013](#)), to average out all other variabilities, in order to obtain the correct beaming amplitude.

3.2 Swift UVOT photometry

The *Neil Gehrels Swift Observatory*⁶ ([Gehrels et al. 2004](#)) obtained 187 short exposures of the active galaxy Mrk 231 over the course of a year, resulting in serendipitous UV measurements of

⁶ <https://swift.gsfc.nasa.gov/>

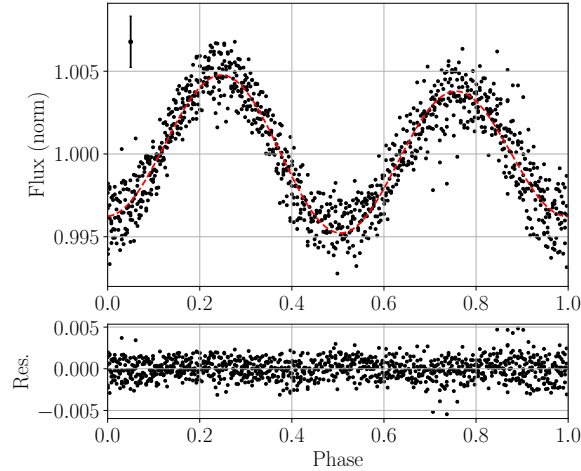


Figure 10. *TESS* photometry from Sector 22, phase-folded with the RV orbital period, showing the ellipsoidal modulation of the F-type star. *Top* — *TESS* data points are in black. Red line is the best-fit two-harmonic model. The typical uncertainty of the data points is plotted in the upper left corner. The ellipsoidal modulation is at half the orbital period. *Bottom* — residuals from the model.

J1255, which was within the field of view of Swift’s UVOT camera in all pointings. Exposure times ranged from ~ 200 s to ~ 1700 s, with a median of ~ 1000 s.

The single UVOT frames were downloaded from HEASARC,⁷ and light curves were extracted with the *photutils* package from *astropy* (Astropy Collaboration et al. 2013), using the optimal aperture (10”) and zero-point magnitude for the *UVM2* filter given by Poole et al. (2008). The resulting light curve, after outlier removal, is composed of 123 individual epochs, all of which are plotted in Fig. 11. A long-term trend, probably due to a slow degradation of the detector, is clearly visible in the data. Similar trend was seen in the intensity of a nearby star. This trend was fitted and removed before a periodic analysis was performed.

To search for any periodic signal in the data we applied the generalized Lomb-Scargle analysis (Zechmeister & Kürster 2009). The resulting periodogram, shown in the upper panel of Fig. 12, exhibits a significant peak at $P = (1.3799 \pm 0.0005)$ d, where the period uncertainty was derived by a Monte Carlo approach. This is in good agreement with half the orbital period of the system, as expected for a system with ellipsoidal modulation.

To derive the shape and amplitude of the modulation, we fitted a two-harmonic model to the phased data, which was normalized to the average flux in that part of the data. We used the orbital period and phase of the RVs, as was done with the *TESS* photometry. The cosine and sine amplitudes of the two harmonics are given in the lower part of Table 3, as was done with the *TESS* data. Also given are the total amplitudes of these two harmonics, A_1 and A_2 .

⁷ <https://heasarc.gsfc.nasa.gov>

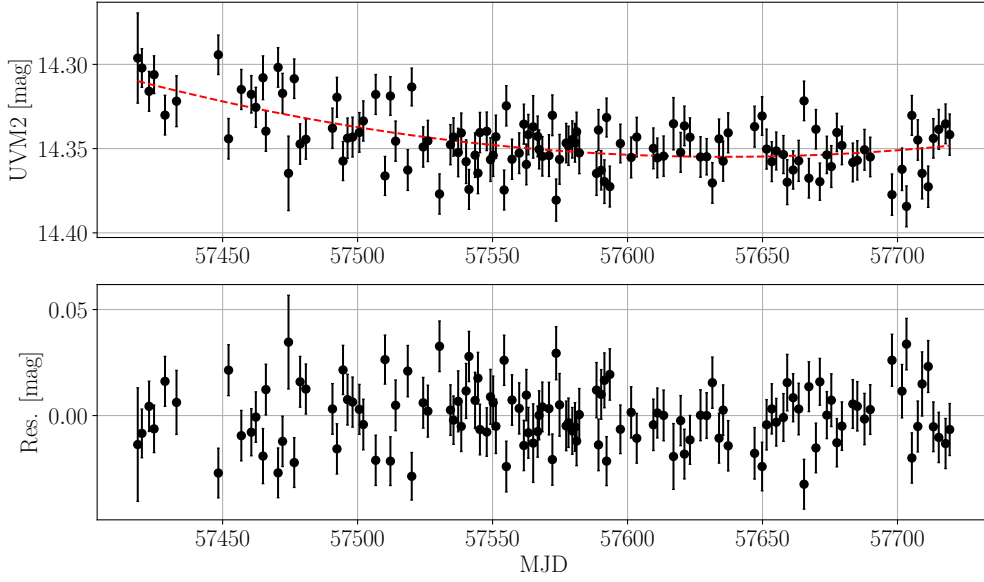


Figure 11. UVOT UVM2 light curve of J1255. *Top* — Original photometry (see text), with a fitted second-order polynomial. *Bottom* — Photometry after the long-term removed.

The shape of the UVM2 modulation, with a deeper minimum at phase ~ 0.5 and a lower maximum at ~ 0.75 , is similar with that of the TESS modulation, with a possible small phase shift; see Section 3.1. The second harmonic amplitude of the UVOT data, 8.4 ± 1.6 ppt, is larger by a factor of two than that of the *TESS* data, although the significance of the difference is only at the 2σ level.

The derived periodogram includes on the order of 100 independent frequencies, and therefore the probability of obtaining the highest peak at the expected frequency, based on the RV and *TESS* photometry is ~ 0.01 . The amplitude we derived is five times larger than its uncertainty, indicating a significance of 5σ . Furthermore, the phase of the modulation is consistent with the optical and RV phase, indicating again that the origin of the UV modulation is similar to that of the optical one.

3.3 XMM-Newton observations of J1255

J1255 was also detected in serendipitously X-rays during three XMM-Newton observations of the galaxy Mrk 231 (observation IDs 0081340201, 0770580401 and 0770580501) (Franceschini et al. 2003; Reynolds et al. 2017), as with the galaxy’s *Swift* UVOT observations (Section 3.2). To check for the presence of any X-ray emission in the 0.2–12 keV range that is in excess of that expected from the F star (e.g., from accretion on to a companion compact object), we derived the X-ray

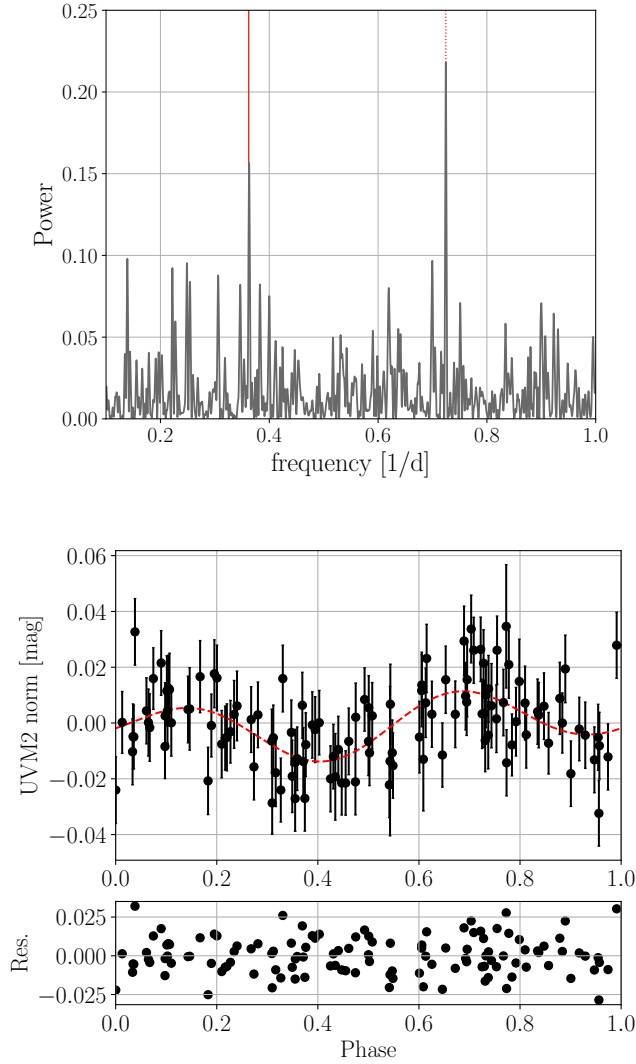


Figure 12. Periodogram and phase-folded UVOT UVM2 light curve. *Top* — GLS periodogram of the normalized flux. The solid and dashed vertical red lines represent the full and half orbital period as determined from the RV data. *Middle* — folded data, with a two-harmonic model at the orbital period. *Bottom* — residuals from the model.

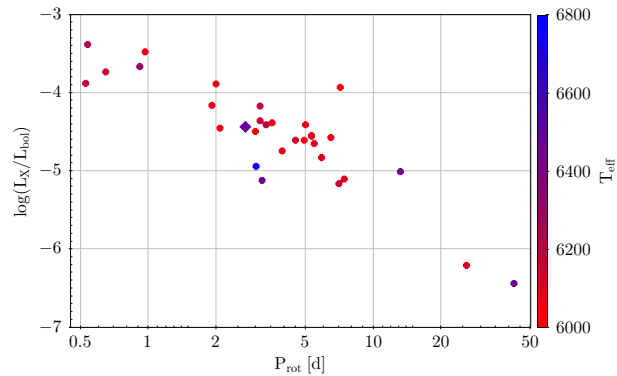


Figure 13. Rotation–X-ray activity relation for F-type stars. The ratio of X-ray to bolometric luminosity vs. rotation periods for 30 stars with similar effective temperatures $6000 \text{ K} \leq T_{\text{eff}} \leq 6800 \text{ K}$, as denoted by their color coding, are plotted from the catalog of [Wright et al. \(2011\)](#). J1255 appears as a diamond.

Table 4. Atmospheric parameters for J1255

	$T_{1,\text{eff}}$ [K]	$\log g$ [c.g.s]	[Fe/H]	$v \sin i_{\text{rot}}$ [km s ⁻¹]
LAMOST	6210	4.10	-0.49	
±	15	0.02	0.01	
TRES	6165	4.30	0.06	34.6
±	50	0.10	0.08	0.6
CARMENES	6280			32.3
±	60			0.5
TIC	6200	3.95	-0.48	
±	140	0.09	0.01	

luminosity for each of the observations as found by [Traulsen et al. \(2020\)](#), yielding an average of $F_X = (1.49 \pm 0.31) \cdot 10^{-14}$ mW/m², corresponding to $L_X = (6.83 \pm 1.41) \cdot 10^{29}$ erg/s, assuming the parallax from the *Gaia* EDR3 catalog ([Brown et al. 2021](#)). With $L_{\text{bol}} = 4.93 L_{\odot}$ from *Gaia*, and scaling to the distance of the target, we get $\log(L_X/L_{\text{bol}}) = -4.46 \pm 0.07$.

We compare the X-ray-to-bolometric luminosity ratio with the rotational periods and L_X/L_{bol} of stars with similar effective temperatures from the catalog published by [Wright et al. \(2011\)](#), assuming the star is tidally locked, and hence has a rotation period equal to the orbital period of the system. The resulting rotation-activity relation, plotted in Fig. 13, shows that J1255 has an X-ray emission that matches that of MS stars of the same spectral type and similar rotation period. We can thus conclude that J1255 does not display any significant excess X-ray emission.

4 STELLAR PARAMETERS OF THE PRIMARY STAR

In this section we estimate the mass, radius, metallicity and age of the J1255 primary F star.

4.1 Atmospheric parameters of J1255

Table 4 lists the atmospheric parameters of J1255, as derived from the TRES and LAMOST spectra, as well as the temperature from TIC. Fig. 14 compares the consistency of the LAMOST parameters with the broad-band photometric spectral energy distribution (SED) of J1255, as collected from VizieR, given here in mag.⁸ It includes photometry from *Gaia*: BP = 12.131 ± 0.020 , G = 11.877 ± 0.020 , RP = 11.468 ± 0.020 ; 2MASS: J = 11.034 ± 0.021 , H = 10.781 ± 0.023 , K_s = 10.732 ± 0.020 ; and WISE: W₁ = 10.685 ± 0.023 , W₂ = 10.696 ± 0.020 ; in which we adopted a minimum uncertainty of 0.02 mag. We plot the original wavelength and flux of an observed

⁸ <http://vizier.unistra.fr/vizier/sed/>

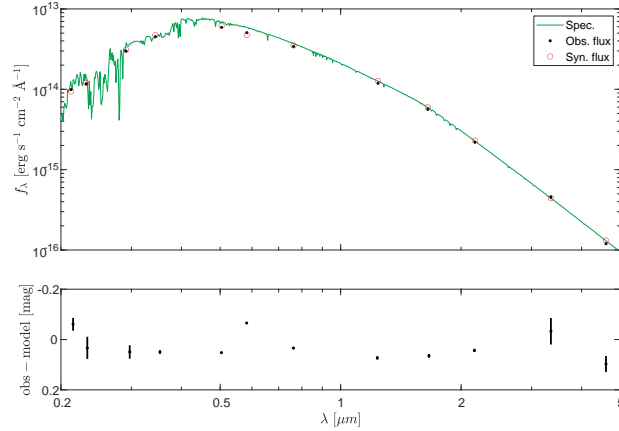


Figure 14. Spectral Energy Distribution of J1255. *Top* — black points are the measured average photometry (from left to right) for the XMM (UVW1, UVM2, UVW2, U), Gaia (BP, G, RP), 2MASS (J, H, K_s) and WISE (W1, W2) bands. Synthetic spectrum and photometry are plotted with a green line and small red circles, respectively, using the atmospheric models of [Castelli & Kurucz \(2003\)](#) with $T_{\text{eff}} = 6250$ K, $\log g = 4$, and metallicity of -0.5 . We adopted here a stellar radius of $R_* = 1.9 R_{\odot}$ at a distance of 600 pc. *Bottom* — photometric residuals, for each filter, in mag.

photometric band for filters having a single measurement, but replace them with weighted-average fluxes and wavelengths for filters with multiple measurements.

Also shown in the figure is a theoretical spectrum from the Spanish Virtual Observatory⁹ (SVO) and synthetic photometry from the folding of this spectrum through the observed bandpasses. No extinction correction is applied, as it is likely quite small (see Table 5 below; A_V is estimated to be less than 0.1). The theoretical spectrum is based on the ATLAS9 stellar atmospheric models of [Castelli & Kurucz \(2003\)](#), which contain synthetic spectra for a three-dimensional grid of effective temperatures, gravities and metallicities. We adopted a grid point that is closest to the stellar parameters derived by LAMOST —effective temperature $T_{\text{eff}} = 6250$ K, $\log g = 4$, and metallicity -0.5 . Based on the parallax of 1.685 mas from *Gaia* ([Gaia Collaboration et al. 2016](#); [Brown et al. 2021](#)), we adopt a stellar radius $R_* = 1.9 \frac{d}{600 \text{ pc}} R_{\odot}$, a value that yields the best fit to the observed broad-band photometry.

Evidently, the theoretical spectrum agrees well with the weighted-averaged photometry. We note, however, that one cannot rule out a contribution to the UV flux from a single WD companion. The flux from even a very hot ($T_{\text{eff}} = 10^5$ K) WD with the smallest mass consistent with our companion-mass constraints (and hence the largest allowed WD radius; $M = 1.1 M_{\odot}$, $\log g = 9$) could still be accommodated within the observed broad-band photometry at the $\sim 10\%$ level. Future FUV observations, at wavelengths where the F-star contribution is negligible, can better rule out hot, massive WD companions.

⁹ <http://svo2.cab.inta-csic.es/theory/main/>

4.2 Stellar parameters of J1255

To estimate the mass, radius, metallicity and age of the primary star, we used the python ISOCHRONES¹⁰ software package (Morton 2015), used by many studies (e.g., Huber et al. 2016; Mathur et al. 2017; Koposov et al. 2020). The software uses the MESA Isochrones and Stellar Tracks (MIST) models (Choi et al. 2016) to determine the stellar physical parameters, based on the observed photometric and spectroscopic parameters. We used the available photometry from the UV to the IR bands, with a prior on temperature and metallicity from the LAMOST spectrum analysis. The SPC analysis (Bieryla et al. 2021; Buchhave et al. 2012) of the TRES spectra, yielded similar results, except for the stellar metallicity, as seen in Table 4. The photometric data were combined with four additional constraints: a parallax of 1.685 ± 0.012 mas (a distance of 595 ± 5 pc), as reported in the *Gaia* EDR3 archival database,¹¹ and the spectroscopic parameters that we used above in Section 4.1: $T_{\text{eff}} = 6250 \pm 100$ K, $\log g = 4.0 \pm 0.1$ and $[\text{Fe}/\text{H}] = -0.50 \pm 0.05$.

The code explores a five-dimensional parameter space of initial mass, stellar age, metallicity, distance and line-of-sight V-band extinction, using an MCMC algorithm, given the priors listed in Table 5. The resulting corner plots for the physical parameters are shown in Figs. 15–16. We note that unlike many X-ray binaries, for which the optical star fills its Roche lobe (e.g., Orosz et al. 2007, 2009), the stellar ellipsoidal shape of J1255 cannot affect our results, as the stellar distortion is minute. The ellipsoidal modulation is less than 0.5%, as a result of the small Roche-lobe filling factor of 0.43 (see Section 5 below).

The adopted parameters of the primary of J1255 are listed in Table 5. We have conservatively assumed that the uncertainties reported by ISOCHRONES are slightly too small, because it ignored some systematic errors, in particular those of the MESA Isochrones and MIST models. We assumed $\sim 5\%$ uncertainty in the primary mass, as the ISOCHRONES estimation depends on stellar models, and $0.05R_{\odot}$ in the stellar radius. The latter is directly constrained by the broad-band photometry and the *Gaia* distance.

To study the Galactic dynamics of J1255, we have derived its Galactic orbit in Appendix A and Fig. A1. The star moves on a constrained Galactic radial orbit between 7.8–10.5 kpc that takes it up and down the plane by $Z \sim 0.6$ kpc. Using estimates of the Galactic velocities, we further find $(U, V, W) = (-35.08 \pm 0.26, 5.99 \pm 0.14, -17.44 \pm 0.28)$ km s⁻¹, suggesting that J1255 has typical thin-disk kinematics (e.g., Bashi & Zucker 2022).

¹⁰ <https://isochrones.readthedocs.io/en/latest/>

¹¹ <https://gea.esac.esa.int/archive/>

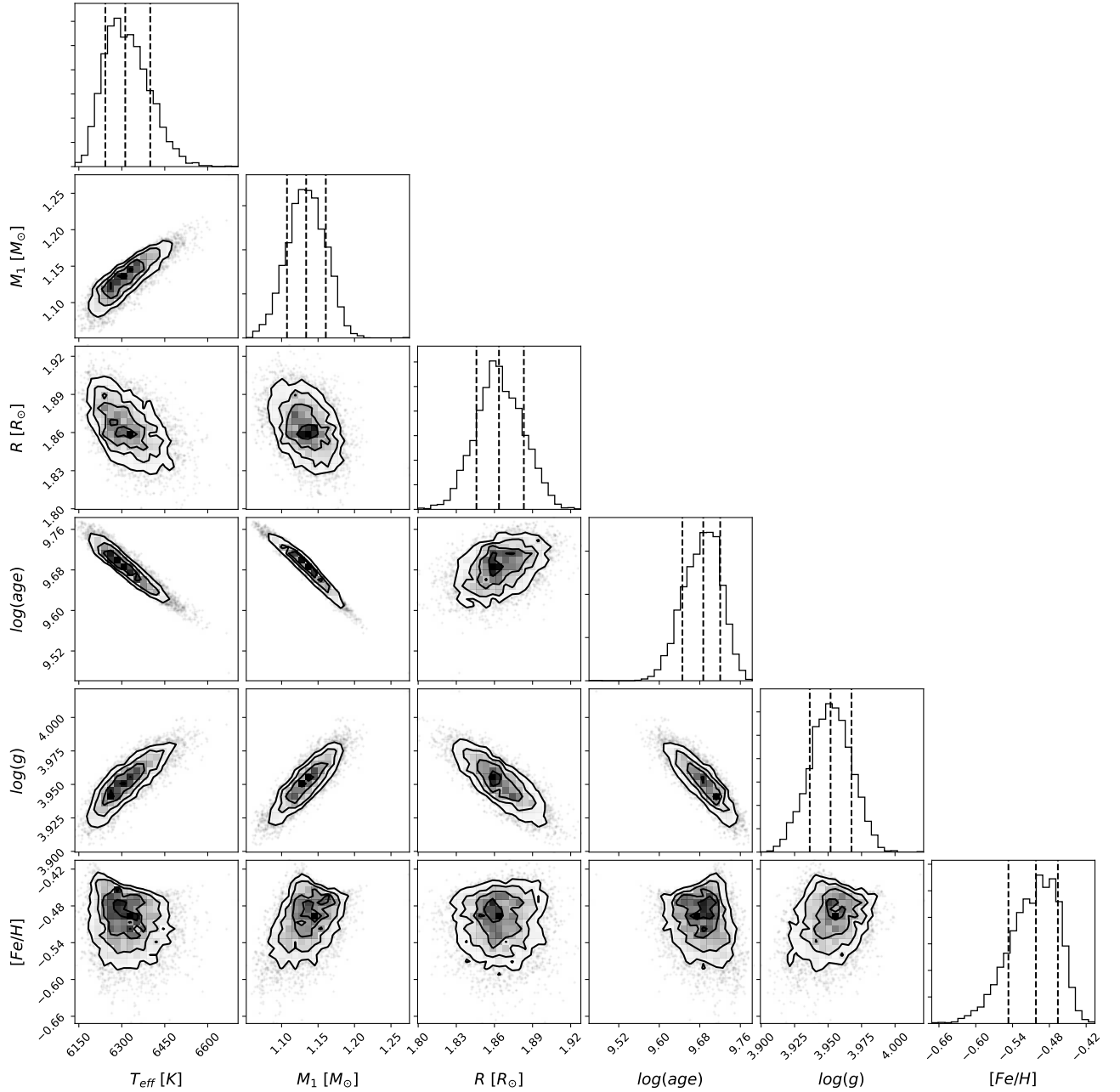


Figure 15. MCMC posterior distributions for the J1255 stellar physical parameters: T_{eff} [K], M_1 [M_{\odot}], R [R_{\odot}], log of stellar age, $\log g$ and $[\text{Fe}/\text{H}]$. See Fig. 6 for details.

5 THE MASS OF THE UNSEEN COMPANION

To derive the mass of the unseen companion, one can use the RV amplitude, which depends, for a circular orbit, on the primary and secondary masses, M_1 and M_2 , the period, P , and the inclination i :

$$K = 213 \left(\frac{M_1}{M_{\odot}} \right)^{1/3} \left(\frac{P}{\text{day}} \right)^{-1/3} \frac{q}{(1+q)^{2/3}} \sin i \text{ km s}^{-1}, \quad (1)$$

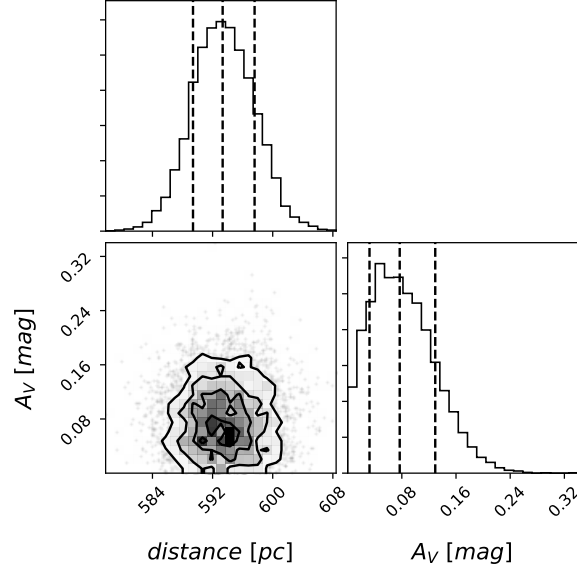


Figure 16. MCMC posterior distributions of J1255 distance and V-band extinction, A_V . See Fig. 6 for details.

Table 5. Adopted Stellar Parameters of the primary of J1255

Parameter	Units	Prior	ISOCHRONES	Adopted
T_{eff}	K	$\mathcal{N}(6250, 100)$	6310^{+90}_{-70}	6300 ± 100
M	M_{\odot}	$\mathcal{U}(1.0, 1.6)$	$1.13^{+0.03}_{-0.02}$	1.13 ± 0.05
R	R_{\odot}	$\mathcal{U}(0, 100)$	$1.86^{+0.02}_{-0.01}$	1.86 ± 0.05
$\log(\text{age})$	yrs	$\mathcal{U}(9, 10)$	$9.69^{+0.03}_{-0.04}$	9.70 ± 0.05
$\log g$	c.g.s.	$\mathcal{N}(4.0, 0.1)$	$3.95^{+0.02}_{-0.01}$	3.95 ± 0.05
[Fe/H]		$\mathcal{U}(-0.75, -0.25)$	$-0.50^{+0.03}_{-0.05}$	-0.50 ± 0.05
Distance	pc	$\mathcal{U}(580.8, 606.0)$	593^{+5}_{-4}	593 ± 10
A_V		$\mathcal{U}(0, 1)$	$0.077^{+0.052}_{-0.045}$	0.08 ± 0.05

where $q \equiv M_2/M_1$. We already derived an estimate for M_1 , so we are left with only one unknown — the orbital inclination, in order to be able to solve for M_2 .

To derive the inclination one can assume the stellar rotation is aligned and synchronized with the orbital motion, as might be expected due to long-term tidal interaction between the close components (e.g., Mazeh 2008). We then compare the observed ellipsoidal-modulation amplitude with theoretical expectations for such a short-period binary, yielding one constraint on the companion mass and orbital inclination. Another constraint can come from the projected equatorial rotational velocity of the F star, which can be determined from the observed spectral-line broadening, provided we know the stellar radius. The advantage of using both constraints, the projected stellar rotation and the ellipsoidal amplitude, is the different dependence of the two on the inclination — while the projected rotational velocity depends on $\sin i$, the ellipsoidal amplitude depends on $\sin^2 i$ (e.g., Morris & Naftilan 1993; Faigler & Mazeh 2011).

In the case of J1255, the *TESS* photometry (Section 3.1) shows a flux modulation of 4.27 ± 0.05 ppt, with a period that is exactly half the RV period, and with a phase that is expected for the ellipsoidal modulation, with no indication of an eclipse. Analysis of the TRES and CARMENES spectra yields an estimation for the projected rotational broadening of 32.3 ± 0.5 km s⁻¹. Neither of these two constraints is iron-clad. The expected ellipsoidal modulation is based on theoretical approximations that are known to fail in reproducing the fine details of the effect (Gomel et al. 2021a), and the determination of the projected equatorial rotation velocity requires assumptions about how to account for line-broadening effects other than rotation (e.g., Barklem et al. 2000; Ryabchikova et al. 2016), and further assumptions about synchronization and alignment of the stellar rotation with the orbital motion. Nevertheless, we have used these two additional constraints with enlarged uncertainties of 10% that reflect these associated open questions.

To obtain the secondary mass and inclination of J1255, we use the PyMC package for probabilistic programming (Salvatier et al. 2016). The search uses uninformative priors on the cosine of the inclination, $\cos i$, and the mass ratio q and the orbital period P , as listed in the top part of Table 6. Given these priors, we calculate the values of secondary mass and inclination by comparing the resulting projected rotational velocity, ellipsoidal amplitude and RV semi-amplitude, as found from Eq. 1 above, together with

$$v \sin i = 50.6 \left(\frac{R_1}{R_\odot} \right) \left(\frac{P}{\text{day}} \right)^{-1} \sin i \quad \text{km s}^{-1}, \quad (2)$$

$$A_2 = 13.44 \alpha \left(\frac{M_1}{M_\odot} \right)^{-1} \left(\frac{R_1}{R_\odot} \right)^3 \left(\frac{P}{\text{day}} \right)^{-2} \frac{q}{1+q} \sin^2 i \quad \text{ppt}, \quad (3)$$

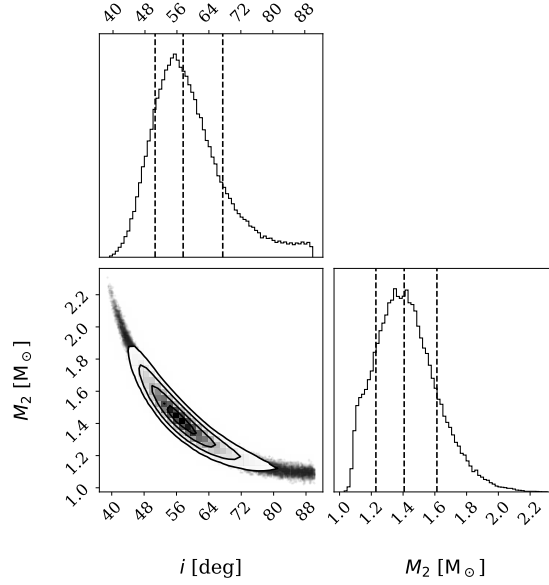
where α is the ellipsoidal coefficient (Faigler & Mazeh 2011; Gomel et al. 2021b), which we set to 1.3, given the temperature of the primary. We then calculated the likelihood of the corresponding observed quantities, assuming the errors are Gaussian and additive, as listed in the lower part of Table 6. We assume the inclinations of the orbit and the stellar rotational axis are both i , and the rotation period and the orbital period both equal P .

Table 6 lists the resulting posterior median and 1σ widths of the system parameters which, based on the adopted uncertainties, are consistent with the input distributions. This indicates the validity of our assumptions, given the problem is over-determined, as we have in hand more constraints than free parameters. In particular, the primary radius turns out to be only 0.166 of the binary separation, and the star fills only 0.43 of its Roche lobe. In such cases, Equation 3 is a very good approximation of the ellipsoidal modulation.

Fig. 17 shows the results of the MCMC process for the companion mass and its orbital inclination.

Table 6. Parameters (priors) used to derive the unseen companion mass and their posterior distributions

Parameter	Units	Prior	Posterior	
Primary mass	M_1	M_\odot	$\mathcal{N}(1.13, 0.05)$	1.16 ± 0.05
Primary radius	R_1	R_\odot	$\mathcal{N}(1.86, 0.05)$	1.82 ± 0.05
Orbital period	P	day	$\mathcal{N}(2.760549, 0.000013)$	2.760549 ± 0.000013
Inclination angle	$\cos i$		$\mathcal{U}(0, 1)$	$0.54^{+0.10}_{-0.16}$
Mass ratio	q		$\mathcal{U}(0.5, 2)$	$1.2^{+0.2}_{-0.17}$
Projected rotational velocity	$v \sin i$	km s^{-1}	32.3 ± 3.0	28.3 ± 2.2
Ellipsoidal amplitude	A_2	ppt	4.27 ± 0.43	4.71 ± 0.36
RV semi-amplitude	K	km/s	96.1 ± 0.2	96.1 ± 0.2


Figure 17. Possible values of the secondary mass vs. the orbital inclination, resulting from the MCMC run. The off-diagonal plot presents the joint distributions with contours, and the diagonal elements show the probability distribution of the two parameters, with percentiles of 16%, 50% and 84%, denoted by vertical dashed lines.

From the 1-d marginalized posterior, the mass estimate for the unseen companion is

$$1.41^{+0.21}_{-0.18} M_\odot. \quad (4)$$

We note that the posterior mass distribution is highly asymmetric, with a sharp drop at $\sim 1.1M_\odot$, and a long tail that extends up to $\sim 2M_\odot$. The 3σ confidence-level mass range is

$$1.07 - 2.08 M_\odot.$$

6 DISCUSSION

We have shown that the unseen companion of J1255 is more massive than the visible F-type star, with a mass of $1.1\text{--}2.1 M_\odot$ at the 3σ confidence level, and a mass-distribution median of $1.4 M_\odot$.

This mass estimate is based on the observed RV modulation, the amplitude of the ellipsoidal modulation, and the rotational broadening of the spectral lines. As emphasized above in Section 5,

the derivation relies on several assumptions, particularly the alignment and synchronization of the primary with the orbital motion, as expected for such a short-period binary (e.g., Mazeh 2008), even more for an *evolving* sub-giant. We further note that the expression used for the expected ellipsoidal modulation is based on theoretical approximations, which is inherently inaccurate to a certain degree (Gomel et al. 2021a). On the other hand, using the ellipsoidal modulation and the rotational broadening constraints makes the problem *over-determined*. The mere existence of a solution for the secondary mass and the inclination is strong evidence that our assumptions are applicable to J1255.

As shown, the synchronization assumption, implying that the F star is rotating around its axis with a period of 2.76 days, can also account for the observed X-ray flux, $\sim 1.5 \times 10^{-14}$ mW/m² (Webb et al. 2020), measured from the XMM-Newton serendipitous observations, as such a flux at the stellar distance is typical for F stars with this rotational period. Another set of serendipitous observations was performed with the *Swift*¹² UVOT telescope (Gehrels et al. 2004) in the UVM2 band, revealing a modulation with the period and phase of the *TESS* modulation, with an amplitude of 8.4 ± 2.1 ppt. The modulation reported here is likely the first detection of an ellipsoidal modulation in the UV.

The stellar UV brightness is coming from the upper layers of the stellar atmosphere, which are tidally distorted by the unseen companion.

6.1 Nature of the more-massive secondary in the J1255 system

Could the more-massive companion in J1255 be another MS star? In such a case we would have seen a second set of spectral lines with the same, or even higher, signal-to-noise ratio than that of the F star. This is especially true for the spectra obtained near quadrature phases, when the two sets of lines would have been well separated, as the RV difference between the two objects is ~ 200 km s⁻¹. No trace of a second star is seen in the TRES and CARMENES spectra, despite their high resolution and high SNR, turning the system to be a single-lined spectroscopic binary (SB1).

SB1 with a mass ratio larger than unity most likely hosts a dormant (i.e. detached non-interacting) compact-object companion, as in a coeval binary with two MS stars, we would expect the more massive star to outshine its companion. The fact that we observe the less massive star in the system suggests that the other star is a compact object.

However, this is not the case for all SB1s. Algol-type binaries, which probably have gone through

¹² <https://swift.gsfc.nasa.gov/>

a mass-transfer phase during their evolution (Erdem & Öztürk 2014; Dervişoğlu et al. 2018; Chen et al. 2020), are famous counterexamples. In these binaries, a giant or a sub-giant is the less-massive component, and yet is the brighter star in the system (Nelson & Eggleton 2001; Budding et al. 2004; Mennekens & Vanbeveren 2017; Negu & Tessema 2018). Therefore, SB1s with a photometric primary in advanced stages of its evolution probably have a more-massive stellar companion as a photometric secondary. Algol-type binaries are much more common than binaries with a neutron-star or a black-hole component.

Indeed, a number of systems recently proposed to consist of an evolved primary and a dormant compact-object secondary (e.g., Thompson et al. 2019; Liu et al. 2019; Rivinius et al. 2020b; Jayasinghe et al. 2021) are more likely to be binaries with an evolved primary and an MS secondary (see discussion by van den Heuvel & Tauris 2020; Irrgang et al. 2020; Shenar et al. 2020; Bodensteiner et al. 2020; Mazeh & Faigler 2020; El-Badry & Quataert 2020; El-Badry et al. 2022a,c). The works of Giesers et al. (2018, 2019), Saracino et al. (2022) and El-Badry et al. (2022b) stand in contrast to most of these recent suggestions, with their primary on the MS, and therefore might have a genuine unseen black-hole companion. J1255 presents us with a similar situation, as demonstrated above, where the secondary cannot be an MS star. In the case of J1255, as the visible star is only slightly evolved, it cannot hide in its glare a MS star with a mass larger than the primary, and therefore the secondary is probably a compact object.

6.2 J1255 secondary — a probable neutron star

The mass we have estimated for the unseen companion in J1255 is within the range of measured masses of confirmed neutron stars

(e.g., Lattimer 2012; Lattimer & Steiner 2014; Özel & Freire 2016).¹³ We therefore argue that the evidence presented here strongly points to a neutron-star companion in J1225.

Could the unseen companion be some other type of compact object? Although the companion is not massive enough to be the BH remnant of a massive star (e.g., Corral-Santana et al. 2016), it could be an unusually massive single white dwarf. A recent analysis of the Gaia EDR3 catalog (Gentile Fusillo et al. 2021) confirms the long-known picture that the mass distribution of white dwarfs in the solar neighborhood has a long tail extending to $1.2M_{\odot}$ and even higher. The range of allowed companion masses in J1255 thus includes the possibility of such a massive white dwarf. Similar ambiguities regarding the identification of a *dormant* neutron star in short-period

¹³ <https://stellarcollapse.org/nsmasses.html>

binaries are bound to affect future similar discoveries, unless deep UV observations can rule out the white-dwarf alternative.

6.3 An inner close binary — an alternative model?

Could the unseen companion in J1225 be, in itself, a close binary with a period of, say, 0.2 d, composed of two low-mass stars, each with a mass of $\gtrsim 0.6M_{\odot}$? The five CARMENES spectra, which include the red part of the spectrum, allow us to explore this possibility. Applying a TODCOR analysis (Zucker & Mazeh 1994a), which is tuned to find secondary lines in a spectrum even when they are faint, we identify no trace of a set of lines typical of M stars, down to a level of 0.5% of the intensity of the F star. This upper limit rules out any M star with a mass exceeding $\sim 0.5M_{\odot}$ (See Appendix B1). Still, one could hypothesize that J1255 is a hierarchical triple system with a close-binary secondary, composed of two or at least one white-dwarf component. For example, two white dwarfs, each with a typical mass of $0.7M_{\odot}$, or a massive white dwarf with a mass of, say, $1M_{\odot}$, and an M star with $0.4M_{\odot}$, are two possibilities that the CARMENES spectra cannot rule out, due to the low-luminosity of the white dwarf and/or the low-mass M star.

Nevertheless, we argue that the scenario in which J1255 is a triple system, where the F star orbits a close binary with a white dwarf as one of its components, is unlikely. Let us first consider the dynamical stability of a hierarchical triple system. The stability depends primarily on $\mathcal{R} = P_3/P_{1,2}$, where $P_{1,2}$ is the orbital period of the close binary and P_3 is that of the wider orbit. Other factors are the mass ratios of the close and wide pairs, the mutual inclination and the eccentricities of the two orbits. Many studies of hierarchical-triple stability suggest that for a system to be stable \mathcal{R} has to be at least 5–10 (e.g., Orlov & Petrova 2000; Mardling & Aarseth 2001). In fact, the known triple systems with short $P_2 \lesssim 0.25$ d all have $\mathcal{R} \gtrsim 100$ (Tokovinin 2018). Triple systems having \mathcal{R} that is too small go through a dynamical interaction that eventually destroys the system (Toonen et al. 2021). This is probably why the most compact known triple systems are with P_3 of ~ 30 d (Tokovinin 2018; Borkovits et al. 2022).

Even if we assume that J1255 is a triple system with an extremely short P_3 of 2.76 d, the stability criterion implies for the presumed close binary of J1255 that $P_{1,2} \lesssim 0.25$ d, or a separation smaller than $\sim 2R_{\odot}$, with a Roche-lobe radius of each of the components on the order of $1R_{\odot}$. To allow some space for the presumed M star, the hypothesized close binary could not be much more compact, unless it is composed of two white dwarfs. A system with $\mathcal{R} \sim 5$ is on the edge of being

stable, and any evolutionary process that slightly decreases \mathcal{R} can render the system dynamically unstable.

In any event, a close binary with a separation of $\sim 2 R_{\odot}$ does not have enough space for a star to evolve through the giant phase and form a white dwarf. Therefore, the original separation of the close binary must have been substantially larger, so that the close binary shrank to its present dimension either by mass transfer or a common envelope phase. Usually, it is expected that in the adiabatic mass-transfer evolution phase of a triple system, the inner orbit shrinks while the outer orbit expands (Toonen et al. 2021), leading to an increase of \mathcal{R} . This means that \mathcal{R} was originally even smaller than its present value. Such a system could not have survived the dynamical interaction between the two orbits.

Another possible route of evolution is that the three stars were engulfed by the expanding atmosphere of the presumed progenitor of the white dwarf and shrank to the present configuration. However, as shown by Comerford & Izzard (2020), who considered the outcome of a triple system in a common-envelope phase, such a system is doomed to be destroyed by the chaotic motion inside the extended envelope.

In summary, it is difficult to imagine an evolutionary path for J1255 that forms such a close hierarchical triple with a white-dwarf component. A scenario that led to a double white-dwarf close binary, with an F star as the tertiary star at a period of 2.76 d is even less probable. We, therefore, conclude that the hierarchical triple-system assumption for J1255, with the secondary being a close binary, is quite unlikely, because of the short orbital period of the F star.

6.4 A wide companion in the system?

Another triple-system possibility we have considered is that the 2.76 d binary is orbited by a faint distant companion. Such a wide companion will not affect the neutron-star conclusion for the companion, but it can put the J1255 binary evolution in a different context. The third star could have been an angular-momentum sink for the short binary, and pushed the J1255 system by tidal friction into a relatively short period (e.g., Mazeh & Shaham 1979; Fabrycky & Tremaine 2007; Naoz et al. 2016). A triple system model for a binary with a neutron star was first suggested by Mazeh & Shaham (1977) for the X-ray binary Her X-1. Although the idea for Her-X1 is probably wrong (e.g., Truemper et al. 1986; Lanzafame et al. 1994), the triple-system model is applicable to several close binaries with a compact companion (e.g., Bailyn 1987; Zdziarski et al. 2007).

We have performed two searches for a hint of a wide companion to J1255, both with negative

results. First, as explained in Section 2.3, we looked for a long-term trend in the RV residuals, with upper limits of $-0.0015 < a < 0.0030 \text{ km s}^{-1}/\text{day}$ at the 2σ level. This rules out a distant M-star companion of $\sim 0.5 M_{\odot}$ up to a distance on the order of 10 au, unless we caught the wide binary in a special orbital phase.

Second, we performed infrared high-resolution adaptive optics (AO) imaging of J1255 at Palomar Observatory with the PHARO instrument (Hayward et al. 2001), using the natural guide star AO system P3K (Dekany et al. 2013), as detailed in Appendix B2. The range of sensitivity to companions is only on the order of >1 arc-sec, equivalent to 600 au at the distance of J1255. This is much larger than the scale expected for wide binaries that could modify the evolution of the close binary by dynamical friction. Nevertheless, a third star at this distance would suggest a more complicated hierarchical system. However, we did not detect any wide companion above the observational threshold detailed in Appendix B2.

The two negative results do not cover the whole range of possible distances of a wide companion, but, nevertheless, are consistent with the postulation that the J1255 binary system does not have a third distant companion.

6.5 The J1255 binary in context

The J1255 system probably consists of an F-type star in orbit with a dormant neutron star, which was in the past a young pulsar. Currently, the optical star is far from filling its Roche lobe, with a filling factor smaller than 0.5 (see Section 5). In the future, when the F star further evolves and transfers mass onto the compact companion, J1255 might turn into a bright X-ray source, and could later even host a millisecond pulsar.

The discovery of this interesting system, devoid of excess X-ray emission, was made possible by the large RV survey performed by the LAMOST multi-object spectrograph, followed by accurate photometry and high-resolution spectroscopy. The discovery relies heavily on the fact that the observed star is only a slightly evolved F star, and not a giant or a supergiant, as in the case of Algol-type binaries (Budding et al. 2004). In systems with evolved stars (Nelson & Eggleton 2001), the bright star can easily hide a MS or sub-giant companion in its glare (e.g., Saracino et al. 2021; El-Badry & Burdge 2021; El-Badry et al. 2022a,c).

We do expect many dormant systems with either a neutron-star or a black-hole companion, as the dormant phases of such binaries are much longer than the young-pulsar and X-ray accretion phases. In our system, for example, the age of the F star, as derived by isochrones, is about 5 Gyr,

while the pulsar phase, during which the object was spinning as a pulsar, is estimated to last on the order of 10–100 million years (e.g., [Phinney & Blandford 1981](#)), and the mass transferring phase of the F star is substantially less than 1 Gyr. To find additional dormant systems one needs similar large RV surveys, as these close binaries are quite rare. Based on our *single* finding, a preliminary guess for the frequency of the dormant short-period systems is on the order of one to a few per million stars.

To find more systems with compact objects one can use the *Gaia* large sample of spectroscopic binaries ([Gaia Collaboration et al. 2022](#)) released very recently, which contains 181 327 orbits, including the orbit of J1255. This sample probably has other systems with compact components, as suggested by the *Gaia* binary paper (but see [El-Badry & Rix 2022](#), for a careful assessment of some of these systems). Another approach is to search for MS stars that exhibit a relatively large ellipsoidal modulation, which, again, might indicate a massive unseen companion ([Gomel et al. 2021c](#)). Photometric light curves are available for a large number of stars ([Rowan et al. 2021](#)), on the order of 10^8 , or even more.

The spectroscopic and the photometric approaches alike necessitate RV follow-up observations to establish the mass of the companion and its nature. With the results of such surveys one will be able to study the frequency and other statistical features of the dormant compact objects, neutron stars and black holes, residing in *close* binary systems. Both populations are important for understanding the evolution of binaries with massive companions (e.g., [Belczynski et al. 2002](#)) that can lead to the generation of neutron stars or black holes, and their possible contribution, in extreme cases, to the merger events detected recently via gravitational waves.

ACKNOWLEDGEMENTS

We thank the anonymous referee for thoughtful comments and suggestions that improved the original manuscript, and H-W Rix for discussion of the beaming modulation. This research was supported by Grant No. 2016069 of the United States-Israel Binational Science Foundation (BSF) to TM, Grant No. I-1498-303.7/2019 of the German-Israeli Foundation for Scientific Research and Development (GIF) to TM and DM, a grant from the European Research Council (ERC) under the European Union’s FP7 Programme, Grant No. 833031 to DM, the National Key R&D Program of China (No. 2019YFA0405100) to SD. The research of NH and SS is supported by a Benozziyo prize postdoctoral fellowship.

This paper uses data from the LAMOST survey: Guoshoujing Telescope (the Large Sky Area

Multi-Object Fiber Spectroscopic Telescope, LAMOST) is a National Major Scientific Project built by the Chinese Academy of Sciences. Funding for the project has been provided by the National Development and Reform Commission. LAMOST is operated and managed by the National Astronomical Observatories, Chinese Academy of Sciences.

This work has also made use of data from the European Space Agency (ESA) mission *Gaia* (<https://www.cosmos.esa.int/gaia>), processed by the *Gaia* Data Processing and Analysis Consortium (DPAC; <https://www.cosmos.esa.int/web/gaia/dpac/consortium>). Funding for DPAC has been provided by national institutions, in particular the institutions participating in the *Gaia* Multilateral Agreement.

This research made use of `exoplanet` (Foreman-Mackey et al. 2021b) and its dependencies (Astropy Collaboration et al. 2013, 2018; Salvatier et al. 2016; Team et al. 2016; Luger et al. 2019; Agol et al. 2020).

DATA AVAILABILITY

Data used in this study are available upon request from the corresponding author.

REFERENCES

- Abdul-Masih M., et al., 2020, *Nature*, **580**, E11
- Agol E., Luger R., Foreman-Mackey D., 2020, *The Astronomical Journal*, **159**, 123
- Antoniadis J., Tauris T. M., Ozel F., Barr E., Champion D. J., Freire P. C. C., 2016, arXiv e-prints, p. [arXiv:1605.01665](https://arxiv.org/abs/1605.01665)
- Astropy Collaboration et al., 2013, *A&A*, **558**, A33
- Astropy Collaboration et al., 2018, *AJ*, **156**, 123
- Bailyn C. D., 1987, *ApJ*, **317**, 737
- Barklem P. S., Piskunov N., O’Mara B. J., 2000, *A&A*, **363**, 1091
- Bashi D., Zucker S., 2022, *MNRAS*, **510**, 3449
- Belczynski K., Kalogera V., Bulik T., 2002, *ApJ*, **572**, 407
- Bhattacharya D., van den Heuvel E. P. J., 1991, *Phys. Rep.*, **203**, 1
- Bieryla A., et al., 2021, in *Posters from the TESS Science Conference II (TSC2)*. p. 124, [doi:10.5281/zenodo.5130626](https://doi.org/10.5281/zenodo.5130626)
- Bodensteiner J., et al., 2020, *A&A*, **641**, A43
- Borkovits T., et al., 2022, *MNRAS*, **510**, 1352
- Bovy J., 2015, *ApJS*, **216**, 29
- Bovy J., Rix H.-W., 2013, *ApJ*, **779**, 115
- Bransgrove A., Levin Y., Beloborodov A., 2018, *MNRAS*, **473**, 2771
- Brown A. G., et al., 2021, *A&A*, **649**, A1
- Buchhave L. A., et al., 2010, *ApJ*, **720**, 1118
- Buchhave L. A., et al., 2012, *Nature*, **486**, 375
- Budding E., Erdem A., Çiçek C., Bulut I., Soyduğan F., Soyduğan E., Bakiş V., Demircan O., 2004, *A&A*, **417**, 263
- Caballero J. A., et al., 2016, in *Observatory Operations: Strategies, Processes, and Systems VI*. p. 99100E, [doi:10.1117/12.2233574](https://doi.org/10.1117/12.2233574)
- MNRAS* **000**, 1–35 (2015)

- Castelli F., Kurucz R. L., 2003, in Piskunov N., Weiss W. W., Gray D. F., eds, Vol. 210, *Modelling of Stellar Atmospheres*. p. A20
([arXiv:astro-ph/0405087](https://arxiv.org/abs/astro-ph/0405087))
- Chen X., Zhang X., Li Y., Chen H., Luo C., Su J., Chen X., Han Z., 2020, *ApJ*, **895**, 136
- Choi J., Dotter A., Conroy C., Cantiello M., Paxton B., Johnson B. D., 2016, *ApJ*, **823**, 102
- Cifuentes C., et al., 2020, *A&A*, **642**, A115
- Claret A., Bloemen S., 2011, *A&A*, **529**, A75
- Comerford T. A. F., Izzard R. G., 2020, *MNRAS*, **498**, 2957
- Corral-Santana J. M., Casares J., Muñoz-Darias T., Bauer F. E., Martínez-Pais I. G., Russell D. M., 2016, *A&A*, **587**, A61
- Cui X.-Q., et al., 2012, *RAA*, **12**, 1197
- Dekany R., et al., 2013, *ApJ*, **776**, 130
- Derişoğlu A., Pavlovski K., Lehmann H., Southworth J., Bewsher D., 2018, *MNRAS*, **481**, 5660
- El-Badry K., Burdge K., 2021, arXiv e-prints, p. [arXiv:2111.07925](https://arxiv.org/abs/2111.07925)
- El-Badry K., Quataert E., 2020, arXiv e-prints, p. [arXiv:2006.11974](https://arxiv.org/abs/2006.11974)
- El-Badry K., Rix H.-W., 2022, arXiv e-prints, p. [arXiv:2206.07723](https://arxiv.org/abs/2206.07723)
- El-Badry K., Seeburger R., Jayasinghe T., Rix H.-W., Almada S., Price-Whelan C. C. A. M., Burdge K., 2022a, *MNRAS*,
El-Badry K., et al., 2022b, arXiv e-prints, p. [arXiv:2209.06833](https://arxiv.org/abs/2209.06833)
- El-Badry K., Burdge K. B., Mróz P., 2022c, *MNRAS*, **511**, 3089
- Erdem A., Öztürk O., 2014, *MNRAS*, **441**, 1166
- Fabrycky D., Tremaine S., 2007, *ApJ*, **669**, 1298
- Faigler S., Mazeh T., 2011, *MNRAS*, **415**, 3921
- Faigler S., Mazeh T., 2015, *ApJ*, **800**, 73
- Faigler S., Mazeh T., Quinn S. N., Latham D. W., Tal-Or L., 2012, *ApJ*, **746**, 185
- Faigler S., Tal-Or L., Mazeh T., Latham D. W., Buchhave L. A., 2013, *ApJ*, **771**, 26
- Faucher-Giguère C.-A., Kaspi V. M., 2006, *ApJ*, **643**, 332
- Feinstein A. D., et al., 2019, *PASP*, **131**, 094502
- Foreman-Mackey D., et al., 2021a, *Journal of Open Source Software*, **6**, 3285
- Foreman-Mackey D., et al., 2021b, *Journal of Open Source Software*, **6**, 3285
- Franceschini A., et al., 2003, *MNRAS*, **343**, 1181
- Furlan E., et al., 2017, *AJ*, **153**, 71
- Gaia Collaboration et al., 2016, *A&A*, **595**, A1
- Gaia Collaboration et al., 2022, arXiv e-prints, p. [arXiv:2206.05595](https://arxiv.org/abs/2206.05595)
- Gehrels N., et al., 2004, *ApJ*, **611**, 1005
- Gentile Fusillo N. P., et al., 2021, *MNRAS*, **508**, 3877
- Giesers B., et al., 2018, *MNRAS*, **475**, L15
- Giesers B., et al., 2019, *A&A*, **632**, A3
- Gomel R., Faigler S., Mazeh T., 2021a, *MNRAS*, **501**, 2822
- Gomel R., Faigler S., Mazeh T., 2021b, *MNRAS*, **501**, 2822
- Gomel R., Faigler S., Mazeh T., Pawlak M., 2021c, *MNRAS*, **504**, 5907
- Gray D. F., 1992, *The observation and analysis of stellar photospheres*. Cambridge university press, pp 386
- Hayward T. L., Brandl B., Pirger B., Blacken C., Gull G. E., Schoenwald J., Houck J. R., 2001, *PASP*, **113**, 105
- Huber D., et al., 2016, *ApJS*, **224**, 2
- Husser T. O., Wende-von Berg S., Dreizler S., Homeier D., Reiners A., Barman T., Hauschildt P. H., 2013, *A&A*, **553**, A6
- Irrgang A., Geier S., Kreuzer S., Pelisoli I., Heber U., 2020, *A&A*, **633**, L5
- Jayasinghe T., et al., 2021, *MNRAS*, **504**, 2577
- Kopal Z., 1959, *Close binary systems*

- Koposov S. E., et al., 2020, *MNRAS*, **491**, 2465
- Lanzafame G., Belvedere G., Molteni D., 1994, *MNRAS*, **267**, 312
- Lattimer J. M., 2012, *Annual Review of Nuclear and Particle Science*, **62**, 485
- Lattimer J. M., Steiner A. W., 2014, *ApJ*, **784**, 123
- Liu J., et al., 2019, *Nature*, **575**, 618
- Luger R., Agol E., Foreman-Mackey D., Fleming D. P., Lustig-Yaeger J., Deitrick R., 2019, *The astronomical journal*, **157**, 64
- Manchester R. N., 2017, *Journal of Astrophysics and Astronomy*, **38**, 42
- Mardling R. A., Aarseth S. J., 2001, *MNRAS*, **321**, 398
- Mathur S., et al., 2017, *ApJS*, **229**, 30
- Mazeh T., 2008, in Goupil M. J., Zahn J. P., eds, *EAS Publications Series Vol. 29*, *EAS Publications Series*. pp 1–65 ([arXiv:0801.0134](https://arxiv.org/abs/0801.0134)), [doi:10.1051/eas:0829001](https://doi.org/10.1051/eas:0829001)
- Mazeh T., Faigler S., 2020, *MNRAS*, **498**, L58
- Mazeh T., Shaham J., 1977, *ApJ*, **213**, L17
- Mazeh T., Shaham J., 1979, *A&A*, **77**, 145
- McQuillan A., Aigrain S., Mazeh T., 2013, *MNRAS*, **432**, 1203
- McQuillan A., Mazeh T., Aigrain S., 2014, *ApJS*, **211**, 24
- Mennekens N., Vanbeveren D., 2017, *A&A*, **599**, A84
- Morris S. L., 1985, *ApJ*, **295**, 143
- Morris S. L., Naftilan S. A., 1993, *ApJ*, **419**, 344
- Morton T. D., 2015, *isochrones: Stellar model grid package (ascl:1503.010)*
- Nagel E., Czesla S., Kaminski A., Zechmeister M., Tal-Or L., Schmitt J. H. M. M., Ribas I., 2022, *A&A*
- Naoz S., Fragos T., Geller A., Stephan A. P., Rasio F. A., 2016, *ApJ*, **822**, L24
- Negu S. H., Tessema S. B., 2018, *Astronomische Nachrichten*, **339**, 709
- Nelson C. A., Eggleton P. P., 2001, *ApJ*, **552**, 664
- Orlov V. V., Petrova A. V., 2000, *Astronomy Letters*, **26**, 250
- Orosz J. A., et al., 2007, *Nature*, **449**, 872
- Orosz J. A., et al., 2009, *ApJ*, **697**, 573
- Özel F., Freire P., 2016, *ARA&A*, **54**, 401
- Paul B., 2017, *Journal of Astrophysics and Astronomy*, **38**, 39
- Phinney E. S., Blandford R. D., 1981, *MNRAS*, **194**, 137
- Poole T. S., et al., 2008, *MNRAS*, **383**, 627
- Quirrenbach A., et al., 2016, in *Ground-based and Airborne Instrumentation for Astronomy VI*. p. 990812, [doi:10.1117/12.2231880](https://doi.org/10.1117/12.2231880)
- Quirrenbach A., et al., 2018, in Evans C. J., Simard L., Takami H., eds, *Society of Photo-Optical Instrumentation Engineers (SPIE) Conference Series Vol. 10702*, *Ground-based and Airborne Instrumentation for Astronomy VII*. p. 107020W, [doi:10.1117/12.2313689](https://doi.org/10.1117/12.2313689)
- Reynolds C., Punsly B., Miniutti G., O’Dea C. P., Hurley-Walker N., 2017, *ApJ*, **836**, 155
- Ricker G. R., et al., 2015, *Journal of Astronomical Telescopes, Instruments, and Systems*, **1**, 014003
- Rivinius T., Baade D., Hadrava P., Heida M., Klement R., 2020a, *A&A*, **637**, L3
- Rivinius T., Baade D., Hadrava P., Heida M., Klement R., 2020b, *A&A*, **637**, L3
- Rowan D. M., Stanek K. Z., Jayasinghe T., Kochanek C. S., Thompson T. A., Shappee B. J., Holoiien T. W. S., Prieto J. L., 2021, *MNRAS*, **507**, 104
- Ryabchikova T., et al., 2016, *MNRAS*, **456**, 1221
- Salvatier J., Wiecki T. V., Fonnesbeck C., 2016, *PeerJ Computer Science*, **2**, e55
- Saracino S., et al., 2021, *MNRAS*,
- Saracino S., et al., 2022, *MNRAS*, **511**, 2914
- Schäfer S., Guenther E. W., Reiners A., Winkler J., Pluto M., Schiller J., 2018, in Evans C. J., Simard L., Takami H., eds, *Society of Photo-Optical Instrumentation Engineers (SPIE) Conference Series Vol. 10702*, *Ground-based and Airborne Instrumentation for Astronomy VII*. p. 1070276,

doi:10.1117/12.2315241

- Shenar T., et al., 2020, *A&A*, 639, L6
- Stassun K. G., et al., 2019, *AJ*, 158, 138
- Tauris T. M., van den Heuvel E. P. J., 2006, Formation and evolution of compact stellar X-ray sources. pp 623–665
- Team T. T. D., et al., 2016, arXiv preprint arXiv:1605.02688
- Thompson T. A., et al., 2019, *Science*, 366, 637
- Tokovinin A., 2018, *ApJS*, 235, 6
- Toonen S., Boekholt T. C. N., Portegies Zwart S., 2021, arXiv e-prints, p. arXiv:2108.04272
- Traulsen I., et al., 2020, *A&A*, 641, A137
- Truemper J., Kahabka P., Oegelman H., Pietsch W., Voges W., 1986, *ApJ*, 300, L63
- Watson M. G., et al., 2009, *A&A*, 493, 339
- Webb N. A., et al., 2020, *A&A*, 641, A136
- Wright N. J., Drake J. J., Mamajek E. E., Henry G. W., 2011, *ApJ*, 743, 48
- Zdziarski A. A., Wen L., Gierliński M., 2007, *MNRAS*, 377, 1006
- Zechmeister M., Kürster M., 2009, *A&A*, 496, 577
- Zucker S., 2003a, *MNRAS*, 342, 1291
- Zucker S., 2003b, *MNRAS*, 342, 1291
- Zucker S., Mazeh T., 1994a, *ApJ*, 420, 806
- Zucker S., Mazeh T., 1994b, *ApJ*, 420, 806
- Zucker S., Mazeh T., Santos N. C., Udry S., Mayor M., 2004, *A&A*, 426, 695
- Zucker S., Mazeh T., Alexander T., 2007, *ApJ*, 670, 1326
- van den Heuvel E. P. J., Tauris T. M., 2020, *Science*, 368, eaba3282

APPENDIX A: J1255 GALACTIC DYNAMICS

To study the Galactic dynamics of J1255 we derived its current Galactic position, using its equatorial coordinates, parallax, and proper motions as given by *Gaia* EDR3 (Brown et al. 2021), and our derived center of mass RV. We used the GALPY package¹⁴ for Galactic motion calculations (Bovy 2015) with the MWPotential2014 approximation for the Milky Way gravitational field (Bovy & Rix 2013) to back-propagate the stellar orbit 4.8 Gyr, using our best estimation of the stellar age.

The resulting Galactic orbit is plotted in Fig. A1. The star moves on a constrained Galactic radial orbit between $R = 7.8\text{--}10.5$ kpc that takes it up and down the plane to a scale height of $Z \sim 0.6$ kpc, well inside the galactic disk.

¹⁴ <https://docs.galpy.org/en/v1.7.1/>

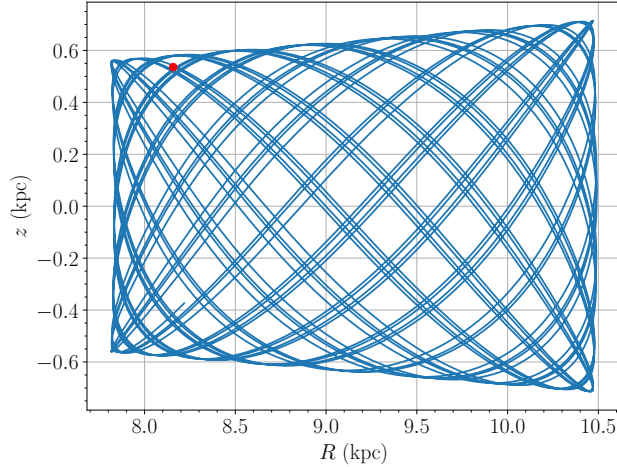


Figure A1. J1255 stellar Galactic scale height above mid plane Z as function of Galactic radii with respect to Galactic center. Blue curve marks the orbit from current position (red point) and back in time for 4.8 Gyr.

APPENDIX B: SEARCHING FOR A FAINT COMPANION OF J1255

B1 Searching for a faint spectroscopic component in the CARMENES spectra

Search for a secondary component in the CARMENES spectra was performed with TODMOR (Zucker 2003b; Zucker et al. 2004), an implementation for multi-order spectra of the two-dimensional cross-correlation method TODCOR (Zucker & Mazeh 1994b). This technique uses two different templates, one for each component, scaled by their flux ratio, to construct a two-dimensional cross correlation as a function of the RVs of the two templates. The peak of the CCF yields the RVs of the two components of the binary.

TODMOR can be used to exclude a faint secondary in the spectrum, as was done here. We inspected the CARMENES spectra with the highest SNR to search for spectral signatures of any companion, using an assortment of templates with a range of 6000–4000 K, obtaining negative results. This included the whole spectra, as well as individual echelle orders, all with the same negative results.

B1.1 Injection-retrieval tests

To quantify the negative result, we performed an injection-retrieval test to determine the limiting flux ratio at which a secondary star could have been detected. We used the highest SNR spectrum from CARMENES, and injected a PHOENIX synthetic spectra of 4000 K, Doppler-shifted at -200 km s^{-1} . The injected spectra were scaled using different flux ratios from 0.5% to 5%, and broadened with the expected rotational projected velocity of a synchronized K7 star, of 10 km s^{-1} .

We inspected the resulting spectra with TODMOR to see if we could detect the injected signal,

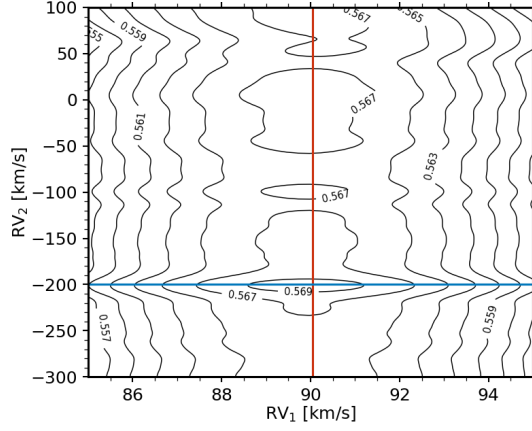


Figure B1. Two dimensional cross-correlation function computed with TODMOR resulting from the injection-retrieval of a secondary spectra with a flux ratio of 2%. The red vertical and blue horizontal lines indicate the RV position of the primary component and that of the injected signal, respectively. The numbers on the contours indicate the height of the CCF.

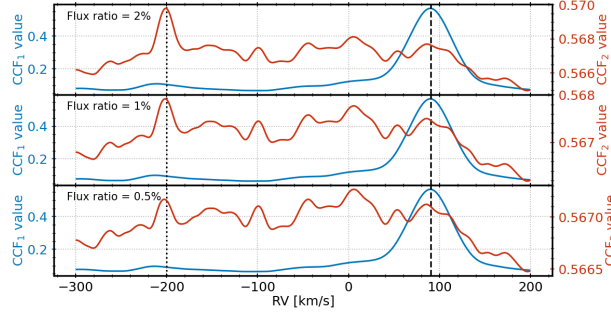


Figure B2. Results from the injection-retrieval of secondary signals with flux ratios of 2% (top), 1% (middle) and 0.5% (bottom). The panels display one-dimensional sections of the two-dimensional CCF computed with TODMOR, corresponding to the vertical red and horizontal blue lines shown in Fig. B1. The dashed and dotted vertical lines indicate the RV positions of the primary component and the injected signal, respectively.

using a primary template with the same parameters as the ones used to compute the RVs, and a secondary template with the parameters used in the injected spectrum.

We show in Fig. B1 the two-dimensional cross correlation obtained with TODMOR for the injection of a spectrum with a flux ratio of 2%, while in Fig. B2 we show the resulting one-dimensional sections of the two-dimensional cross correlation, computed for injected spectra with three different flux ratios. For the spectra with injected flux ratios of 2% and 1%, the CCF peak of the secondary component (red) is located at the radial velocity of the injected signal, and is easily detected. The signal produced by an injected spectrum with a flux ratio of 0.5% is of the same height as some of the peaks of the surrounding noise, and therefore we consider that flux ratio as barely detectable.

As a result of these tests, we constrain the flux ratio of the unseen companion of J1255 to be lower than 1%. This upper limit rules out any main-sequence (MS) companion with a temperature larger than ~ 3700 K, which have typical masses of $\sim 0.5 M_{\odot}$ (Cifuentes et al. 2020).

B2 Searching for a faint wide component around J1255 with Palomar Adaptive Optics

To search for a faint wide companion to J1255 we obtained high-resolution imaging of J1255 with the infrared high-resolution adaptive optics (AO) imaging at Palomar Observatory, with the PHARO instrument (Hayward et al. 2001) at the 200-inch PALOMAR telescope, behind the natural guide star AO system P3K (Dekany et al. 2013), on 2021 Feb 23 UT in a standard 5-point quincunx dither pattern with steps of 5 arc-sec. Each dither position was observed three times, offset in position from each other by 0.5 arc-sec for a total of 15 frames.

The camera was in the narrow-angle mode with a full field of view of ~ 25 arc-sec and a pixel scale of approximately 0.025 arc-sec per pixel. Observations were made in the narrow-band Br- γ filter ($\lambda_o = 2.1686$; $\Delta\lambda = 0.0326\mu\text{m}$) and in the narrow-band $H - cont$ filter ($\lambda_o = 1.668$; $\Delta\lambda = 0.018\mu\text{m}$), each with an integration time of 30 seconds per frame (150 seconds total on-source time).

The AO data were processed and analyzed with a custom set of IDL tools. The science frames were flat-fielded and sky-subtracted. The flat fields were generated from a median average of dark subtracted flats taken on-sky. The flats were normalized such that the median value of the flats is unity. The sky frames were generated from the median average of the 15 dithered science frames; each science image was then sky-subtracted and flat-fielded. The reduced science frames were combined into a single combined image using an intra-pixel interpolation that conserves flux, shifts the individual dithered frames by the appropriate fractional pixels, and median-coadds the frames. The final resolution of the combined dither was determined from the full-width half-maximum of the point spread function; 0.099 arc-sec (60au) in Br- γ and 0.082 arc-sec (49 au) in $H - cont$ (Fig. B3 for $H - cont$; similar results for Br- γ).

The sensitivities of the final combined AO image were determined by injecting simulated sources azimuthally around the primary target every 30° at separations of integer multiples of the central source's FWHM (Furlan et al. 2017). The brightness of each injected source was scaled until standard aperture photometry detected it with 5σ significance. The resulting brightness of the injected sources relative to the target set the contrast limits at that injection location. The final 5σ limit at each separation was determined from the average of all of the determined limits at that separation and the uncertainty on the limit was set by the rms dispersion of the azimuthal slices at a given radial distance (Fig. B3). The only other star detected is 12 arc-sec to the southwest; this star is TIC 150388417 (*Gaia* DR3 1577114984684273664) and has a distance of 350 pc and is thus

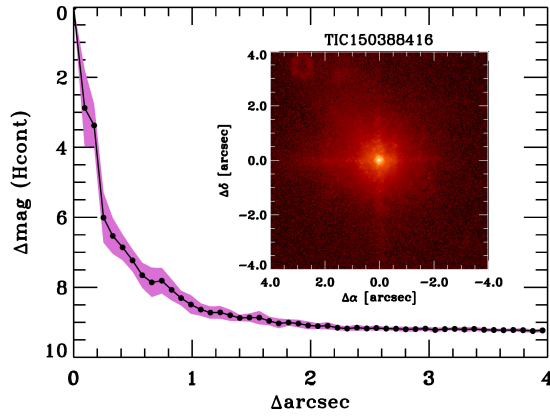


Figure B3. Companion sensitivity for the Palomar adaptive optics imaging of the $H - cont$. The black points represent the 5σ limits and are separated in steps of 1 FWHM; the purple represents the azimuthal dispersion (1σ) of the contrast determinations (see text). The inset image is of the primary target, showing no additional companions to within 3 arc-sec of the target in either filter.

physically unrelated to J1255. There is no evidence in either filter for an additional companion of J1255.

This paper has been typeset from a $\text{\TeX}/\text{\LaTeX}$ file prepared by the author.